Journal of Computational Physics 229 (2010) 6853–6873

Contents lists available at ScienceDirect

Journal of Computational Physics

journal homepage: www.elsevier.com/locate/jcp

Simulation of axisymmetric jets with a finite element Navier–Stokes solver and a multilevel VOF approach

A. Cervone, S. Manservisi *, R. Scardovelli

DIENCA, Montecuccolino Laboratory, University of Bologna, Via dei Colli 16, 40136 Bologna, Italy

ARTICLE INFO

Article history:
Received 7 April 2009
Received in revised form 25 February 2010
Accepted 22 May 2010
Available online 2 June 2010

Keywords:
Jet simulation
Volume-of-fluid
Finite element
Multilevel approach

ABSTRACT

A multilevel VOF approach has been coupled to an accurate finite element Navier–Stokes solver in axisymmetric geometry for the simulation of incompressible liquid jets with high density ratios. The representation of the color function over a fine grid has been introduced to reduce the discontinuity of the interface at the cell boundary. In the refined grid the automatic breakup and coalescence occur at a spatial scale much smaller than the coarse grid spacing. To reduce memory requirements, we have implemented on the fine grid a compact storage scheme which memorizes the color function data only in the mixed cells. The capillary force is computed by using the Laplace–Beltrami operator and a volumetric approach for the two principal curvatures. Several simulations of axisymmetric jets have been performed to show the accuracy and robustness of the proposed scheme.

1. Introduction

A stream of liquid matter that enters a gas region and breaks into small liquid masses is a very complex phenomenon that can occur in many natural and engineering processes. In nature, jets appear on very different spatial scales, ranging from galaxies to atoms. In industrial applications, many devices require the injection of liquid or gas phases as essential part of the combustion process or as primary coolant for heat removal. The dynamics of a liquid jet is rather sensitive to the boundary conditions, to the turbulence inside the liquid and to the surrounding gas and, in spite of large efforts, the mechanisms leading to small fluid structures and droplets are still an open question and object of active research. In recent time, many studies have investigated jets with direct numerical simulations, using the Volume-of-Fluid (VOF), level set and front tracking methods. Front tracking is based on the Lagrangian advection of marker particles that are attached to the interface, while VOF methods rely on the advection of the volumetric fraction of the reference phase in the grid cells. In the level set method the interface is given by the zero-level isosurface of a continuous function defined by the signed distance to the interface. Overviews of several front tracking and front capturing methods can be found in [1,2] for the front tracking, and in [3,4] for the VOF and level set methods, respectively. Realistic spatial simulations are those involving jets entering at one boundary of the computational domain and developing several instabilities in its interior. The simulation of a three-dimensional turbulent jet entering a gas environment, with a uniform discretization of the domain, can be found in [5], an example that illustrates the considerable power of front capturing methods. Other examples can be found in [6–10] or in the reviews [11,12] and citations therein.

One of the most popular method to track the interface is the VOF technique. In this method the interface is reconstructed from the color function data representing the fraction of each grid cell which is occupied by the reference fluid phase. The calculation of the interface geometrical properties, i.e. the local normal and curvature, cannot always be performed

* Corresponding author. Tel.: +39 051 644 1718; fax: +39 051 644 1747.
E-mail address: sandro.manservisi@mail.ing.unibo.it (S. Manservisi).

0021-9991/$ - see front matter © 2010 Elsevier Inc. All rights reserved.
doi:10.1016/j.jcp.2010.05.025

accurately with a fixed number of cells (a 3×3 block of cells in two dimensions and $3 \times 3 \times 3$ cells in three dimensions) by using standard methods, such as the Parker and Youngs' reconstruction or the height function method. For this reason, either smoothing strategies or more complex algorithms with a variable element cell support must be adopted [13,14]. The VOF method has the potential of an exact conservation of the mass if the advection of the color function is performed correctly and there is essentially no limit to the complexity of the interface, since breakup and merging events are handled automatically. However, this implicit treatment of the changes in interface topology does not necessarily imply that they represent the physical reality. For these reasons adaptive grid methods have also been developed, where the domain discretization is adjusted to follow in a more accurate way the different spatial scales and the temporal evolution of the flow structures [15–18].

The computation of the singular capillary force is usually a rather delicate task since the local lack of balance with the pressure gradient is at the origin of the so-called spurious currents which can affect the interface dynamics, both with the continuum surface force (CSF) method [19], and the ghost fluid method (GFM) [20], that imposes sharper boundary conditions on the interface. However, several improvements have been accomplished in the last years with finite volumes and the fractional-step pressure-correction method to integrate in time the Navier–Stokes equations. Firstly, with the incremental form of the predictor step [21], the pressure gradient and the capillary force partially balance each other, and exactly for the spatially-continuous equations in the case of Laplace's law. Secondly, the balanced-force approach has shown that spurious currents are greatly reduced if the pressure gradient and the capillary force are estimated at the cell faces and if the spatial discretization of these two terms is consistent [22,23,14]. More particularly, for a circular droplet Laplace's law is exactly satisfied if the analytical curvature is used, while the system relaxes by viscous damping towards a numerical equilibrium [14] when the curvature is estimated with the height function method. In this case the initial perturbation is determined by the numerical approximation of the curvature which is not constant along a circular interface.

In previous papers [24,25] we have shown that no spurious currents are generated also with a finite element approach if the analytical curvature is considered. In this framework Laplace's law is readily recovered and the force balance on the cell faces is implemented in a natural way with the integration by parts of the Navier–Stokes equations. In this paper we propose a multilevel VOF approach combined with a FEM flow solver that improves the representation of the interface by using more than one linear interface in each cell of the coarse grid, assuring in this way that the automatic breakup and merging events occur at spatial scales smaller than the coarse grid spacing. This paper addresses mainly situations where the spatial scales of the flow are fully resolved but the interface still requires a higher resolution. These situations are rather common, for example a circular fluid body requires a radius of curvature bigger than five grid spacings even in very simple flows, such as translations and solid-body rotations, in order not to be distorted to such an extent that the normal and curvature computations are not enough accurate. In these conditions the grid refinement necessary for the VOF algorithm would be too heavy when extended to the pressure and velocity fields. The multilevel approach reduces the interface discontinuity at the boundary of the cells of the coarse grid by increasing the actual resolution, and it computes more accurately the capillary force on the interface. As a result the balance between discontinuous forces and singular terms is more precise and spurious currents are reduced. The use of an auxiliary mesh to compute a number of geometrical and physical quantities is not new but it has been used to improve the evaluation of the normal, curvature and surface tension stresses [26,27].

The approach presented in this paper is somewhat similar to an adaptive refinement method, however it differs deeply as the mesh subdivisions are only virtual and it does not require any effort for the modification of the mesh, and any extra storage and communication of the flow variables between different levels. In some cases, when the interfacial curvature varies over orders of magnitude and all the different scales need to be resolved, this methodology becomes clearly inefficient if compared to an adaptive mesh refinement and it should be combined with some other approach. However in many cases this further refinement, with respect to the velocity and pressure spatial scales, is required more or less uniformly along the interface for a smoother representation of the interface itself [27]. Since the number of cells cut by the interface is usually very low with respect to the total number of cells of the very refined grid, we have implemented a sparse matrix approach in order to achieve a very compact memorization of the color function data at the highest resolution. In this study we consider the evolution of an axisymmetric jet in cylindrical coordinates. The principal curvature in the r, z plane is computed with the Laplace–Beltrami operator, the other curvature is computed on the interface and then extended radially for the volumetric computation of the capillary force.

In Section 2 we introduce the governing equations and discuss the variational formulation and the multilevel approach. In Section 3 we present the compact storage scheme of the color function data on the fine grid and the numerical implementation of the capillary force. In Section 4 we first validate our approach against the analytical linear dispersion relation for jets and then present the results of the simulations of an axisymmetric jet injected in a gas environment, with different frequencies and inlet velocities. Finally we present our conclusions.

2. Governing equations, variational formulation and finite element model

2.1. Governing equations

In Fig. 1 we consider a typical situation where an axisymmetric liquid jet (reference phase) is injected in a gas environment (secondary phase). Let $\Omega \subset R^3$ be a cylindrical domain with boundary Γ which contains an inlet area, $\Gamma_{in} \subset \Gamma$, and an

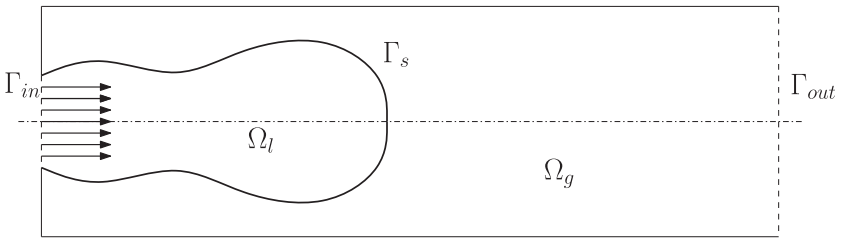

Fig. 1. Domain.

outlet, $\Gamma_{out} \subset \Gamma$. The liquid phase is located in $\Omega_l(t)$ with boundary Γ_l, surrounded by the gas in $\Omega_g(t) = \Omega - \Omega_l(t)$. The interface between the two immiscible fluids is denoted by $\Gamma_s \subset \Gamma_l$.

The liquid distribution in the domain Ω is defined by its characteristic function χ, that changes discontinuously across the interface from the value one in Ω_l to zero.

Since each fluid phase does not change by following the fluid paths, the function χ behaves like a passive scalar and satisfies a simple advection equation

$$\frac{\partial \chi}{\partial t} + (\mathbf{u} \cdot \nabla)\chi = 0. \tag{1}$$

The velocity $\mathbf{u}$ and pressure field p obey the single-fluid formulation of the Navier–Stokes equations, given by the momentum conservation equation

$$\rho \frac{\partial \mathbf{u}}{\partial t} + (\mathbf{u} \cdot \nabla)\mathbf{u} = -\nabla p + \nabla \cdot \mathbf{T} + \mathbf{F} + \mathbf{F}_s \tag{2}$$

and the incompressibility constraint

$$\nabla \cdot \mathbf{u} = 0. \tag{3}$$

The above equations are solved in the computational domain Ω at times $0 \leqslant t \leqslant T$, with appropriate initial and boundary conditions. For simplicity, we consider Dirichlet boundary conditions at the inlet Γ_{in} and homogeneous Neumann boundary conditions at the outlet Γ_{out}. In these equations, the rate-of-strain tensor $\mathbf{D}(\mathbf{u})$ is defined by

$$D_{ij} = \frac{1}{2}\left(\frac{\partial u_i}{\partial x_j} + \frac{\partial u_j}{\partial x_i}\right) \tag{4}$$

and the corresponding stress tensor $\mathbf{T}(\mathbf{u})$ by

$$T_{ij} = 2\mu D_{ij} = \mu\left(\frac{\partial u_i}{\partial x_j} + \frac{\partial u_j}{\partial x_i}\right). \tag{5}$$

The two fluid phases have both constant density, ρ_l and ρ_g, and dynamical viscosity, μ_l and μ_g, respectively. The density ρ and viscosity μ in (2) are functions of χ

$$\rho = \chi\rho_l + (1-\chi)\rho_g, \quad \mu = \chi\mu_l + (1-\chi)\mu_g. \tag{6}$$

The term $\mathbf{F}$ is the given external body force (e.g. gravity) and $\mathbf{F}_s$ is the force acting on the interface Γ_s expressed as a force per unit length [28]

$$\mathbf{F}_s(\mathbf{x}) = \int_{\Gamma_s} \sigma\kappa\mathbf{n}\delta(\mathbf{x} - \mathbf{x}_s)dS, \tag{7}$$

where $\mathbf{x}_s$ are points on Γ_s,σ is the surface tension coefficient, $\mathbf{n}$ the unit external normal, κ the sum of the principle curvatures (in our convention $\kappa < 0$ for a liquid drop) and $\delta(\mathbf{x})$ the volumetric Dirac delta function. In our model the surface tension coefficient is constant, so we do not consider possible variations of σ along the interface line due to temperature gradients or other effects. The normal $\mathbf{n}$, the curvature κ and the interface Γ_s are all geometrical quantities that can be evaluated from a given χ distribution.

2.2. Variational formulation

Since Eqs. (1)–(3) are not always properly defined in standard functional spaces due to the presence of distributions and discontinuous functions, we reformulate the problem in variational form. We denote by $H^d(\Omega), d \geqslant 0$, the Sobolev space of all functions having square integrable derivatives up to order d on Ω and with $\|\cdot\|_d$ and $(\cdot,\cdot)_d$ the standard Sobolev norm and inner product. When $d = 0$, we write $L^2(\Omega)$ instead of $H^0(\Omega)$ and drop the index from the inner product notation. For vector-valued functions and spaces, we use boldface characters. For example, $\mathbf{H}^d(\Omega)$ denotes the space of vector-valued functions

such that each component belongs to $H^d(\Omega)$. Of special interest are the spaces $\mathbf{H}^1(\Omega)$, equipped with the norm $\|\mathbf{v}\|_1 = \left(\sum_{j=1}^{2} \|v_j\|^2\right)^{1/2}$, and $L_0^2(\Omega)$, the space of square integrable functions having zero mean over Ω. Because of the Dirichlet boundary condition on Γ_{in}, we also introduce the subspace $\mathbf{H}^1_{\Gamma_{in}}(\Omega) \subset \mathbf{H}^1(\Omega)$ of functions which are vanishing on Γ_{in}, and $\mathbf{H}^{1/2}(\Gamma_{in})$, which is the space containing all the restrictions of $\mathbf{H}^1(\Omega)$ to the boundary Γ_{in}. With this notation we introduce the continuous bilinear and trilinear forms

$$\begin{aligned} a(\mu, \mathbf{u}, \mathbf{v}) &= 2\int_\Omega \mu \mathbf{D}(\mathbf{u}) : \mathbf{D}(\mathbf{v})\, dV, \\ b(q, \mathbf{v}) &= -\int_\Omega q \nabla \cdot \mathbf{v}\, dV, \\ c(\rho, \mathbf{w}, \mathbf{u}, \mathbf{v}) &= \int_\Omega \rho(\mathbf{w} \cdot \nabla)\mathbf{u} \cdot \mathbf{v}\, dV, \end{aligned} \tag{8}$$

$\forall \mathbf{u}, \mathbf{v}, \mathbf{w} \in \mathbf{H}^1(\Omega)$ and $\forall q \in L_0^2(\Omega)$. The density ρ and the viscosity μ, which are positive function in $L^\infty(\Omega)$, have been defined in (6). For details about the function spaces we have introduced and the bilinear and trilinear forms and their properties, one may consult [29,30].

The weak form of the two-phase Navier–Stokes equation, can be obtained by multiplying (2) with a test function $\mathbf{v}$ and by integrating over the domain Ω

$$\left(\rho \frac{\partial \mathbf{u}}{\partial t}, \mathbf{v}\right) + c(\rho, \mathbf{u}, \mathbf{u}, \mathbf{v}) + b(p, \mathbf{v}) + a(\mu, \mathbf{u}, \mathbf{v}) = (\mathbf{F}, \mathbf{v}) + (\mathbf{F}_s, \mathbf{v}) \tag{9}$$

for any test function $\mathbf{v} \in \mathbf{H}^1_{\Gamma_{in}}(\Omega)$. In a similar way the constraint (3) becomes

$$b(q, \mathbf{u}) = 0 \tag{10}$$

for any test function $q \in L_0^2(\Omega)$. The gravity term is defined by

$$(\mathbf{F}, \mathbf{v}) = (\rho \mathbf{g}, \mathbf{v}) \tag{11}$$

and the surface tension by

$$(\mathbf{F}_s, \mathbf{v}) = \int_{\Gamma_s} \sigma \kappa \mathbf{n} \cdot \mathbf{v}\, dS. \tag{12}$$

To evaluate the above interface integral, we first replace the curvature term by the Laplace–Beltrami operator

$$\nabla_s = (I - \mathbf{nn}) \cdot \nabla \tag{13}$$

and then integrate by parts on $\Gamma(t)$

$$(\mathbf{F}_s, \mathbf{v}) = \int_{\Gamma_s} \sigma \kappa \mathbf{n} \cdot \mathbf{v}\, dS = \int_{\Gamma_s} \sigma \nabla_s^2 \mathbf{x}_s \cdot \mathbf{v}\, dS = -\int_{\Gamma_s} \sigma \nabla_s \mathbf{x}_s : \nabla_s \mathbf{v}\, dS, \tag{14}$$

where we have used the relation $\kappa \mathbf{n} = \nabla_s^2 \mathbf{x}_s$. Since we consider only closed interfaces or open interfaces coupled with Dirichlet boundary conditions, any integral over the boundary of the interface is zero.

The advection equation for χ can be written in variational form by multiplying (1) with the test function $\varphi \in C_0^\infty(\Omega)$ and by applying the divergence theorem

$$\frac{\partial}{\partial t}\int_\Omega \chi \varphi\, dV + \int_\Gamma \chi(\mathbf{u} \cdot \mathbf{n})\varphi\, dS - \int_\Omega \chi \mathbf{u} \cdot \nabla \varphi\, dV = 0. \tag{15}$$

2.3. Finite element discretization and multilevel approach

In numerical approximations we seek solutions in families of finite element spaces. Let us introduce a finite element discretization of the Cartesian domain Ω through the mesh parameter h which tends to zero. We subdivide Ω into a family of squares of side h which obeys to finite element compatibility constraints on their boundary. Let $\mathbf{X}_h \subset \mathbf{H}^1(\Omega)$ and $S_h \subset L_0^2(\Omega)$ be two families of finite dimensional subspaces parameterized by the length h. For $\mathbf{X}_h$ and S_h we use standard quadrangular Taylor–Hood spaces which satisfy the usual compatibility assumptions and the LBB condition. We denote with $\mathbf{u}_h$ and $\mathbf{v}_h$ the solution and any test function in $\mathbf{X}_h$ and with p_h and q_h the solution and any test function in S_h, respectively. The finite element Navier–Stokes system becomes

$$\left(\rho \frac{\partial \mathbf{u}_h}{\partial t}, \mathbf{v}_h\right) + c(\rho, \mathbf{u}_h, \mathbf{u}_h, \mathbf{v}_h) + b(p_h, \mathbf{v}_h) + a(\mu, \mathbf{u}_h, \mathbf{v}_h) = (\mathbf{F}_s, \mathbf{v}_h) + (\mathbf{F}, \mathbf{v}_h), \quad b(q_h, \mathbf{u}_h) = 0. \tag{16}$$

In the remaining of the paper we suppress the h subscript. Now, by starting at the coarse level (c), we subdivide each square of side h in the Cartesian grid Ω^c in smaller squares by using the simple midpoint refinement rule up to a fine level (f), with $f = c + l$. We indicate with $\mathbf{X}^c$, S^c and $\mathbf{X}^f$, S^f the families of subspaces defined at the coarse and fine levels and with Ω_i^c and Ω_i^f the

corresponding generic cell. We introduce also the space of the piecewise constant functions P^f, which is the span of the set of all unitary constant functions with compact support over Ω_i^f and define the color (volume fraction) function in any cell at level (f) as

$$C_i^f = \int_\Omega \chi \varphi_i^f \, dV \tag{17}$$

with $\varphi_i^f \in P^f$. Eq. (15) then becomes

$$\frac{\partial C_i^f}{\partial t} + \int_{\Gamma_i^f} \chi(\mathbf{u}\cdot\mathbf{n}) dS = 0, \tag{18}$$

where Γ_i^f is the boundary of the cell Ω_i^f. Eq. (17) is the standard definition of the VOF color function and (18) the corresponding advection equation [31,32].

Let us consider a two level scheme, where at the fine level the advection equation is solved geometrically for the color function C_i^f, while at the coarse level we take into account only large phase structures to compute the pressure and velocity fields. We introduce also the concept of transfer operators from the fine to the coarse levels of refinement. If some phase structure is present only at the fine level (f), then the solution $(p^c, \mathbf{u}^c)$ at the coarse level is different from $(p^f, \mathbf{u}^f)$, which satisfies the Navier–Stokes equations with different test functions. In order to compute the transfer operators we consider first equation (10) and assume that is satisfied by the velocity field at both levels, i.e. $b(q^f, \mathbf{u}^f) = b(q^c, \mathbf{u}^c) = 0$. We then substitute in the relation at the fine level the coarse velocity field $\mathbf{u}^c$ to get

$$b(q^f, \mathbf{u}^c) = \int_\Omega q^f R^{fc}(\mathbf{u}^c, \mathbf{u}^f) dV, \tag{19}$$

where the fine-to-coarse mass transfer operator R^{fc} is defined by

$$R^{fc}(\mathbf{u}^f, \mathbf{u}^c) = \nabla\cdot(\mathbf{u}^f - \mathbf{u}^c). \tag{20}$$

The transfer operator R^{fc} defines the residual error of (10) when the velocity field solution at the fine level is estimated by $\mathbf{u}^c$. We remark that, even if the discrete solutions are divergence-free functions over the finite element mesh, the pointwise divergences $\nabla\cdot\mathbf{u}^f$ and $\nabla\cdot\mathbf{u}^c$ may be different from zero for all $\mathbf{x}\in\Omega$. As a matter of fact, the divergence-free constraints are $\int_\Omega q^f \nabla\cdot\mathbf{u}^f dV = 0$ and $\int_\Omega q^c \nabla\cdot\mathbf{u}^c dV = 0$, but in general $\int_\Omega q^f \nabla\cdot\mathbf{u}^c dV \neq 0$. In our geometry, the mesh at the fine level (f) is obtained by midpoint refinement from the coarse level (c), then $S^c(\Omega)\subset S^f(\Omega)$ and any test function q^c can be written as a linear combination of the test functions q^f at the fine level. Therefore, the relation $b(q^c, \mathbf{u}^f) = 0$ is clearly verified and

$$0 = b(q^c, \mathbf{u}^c) = b(q^c, \mathbf{u}^c - \mathbf{u}^f) = \int_\Omega q^c R^{fc}(\mathbf{u}^c, \mathbf{u}^f) dV. \tag{21}$$

Under the above assumptions, there is no net mass transfer from the fine to the coarse level. In actual computations we solve only the velocity field at the coarse level and we project it to the fine level to advect the color function. If the projection does not preserve the divergence-free constraint, then the transfer operator is not zero and it must be taken into account as an artificial source.

Now we estimate the momentum equation error of the two–level scheme. Let $(p^f, \mathbf{u}^f)$ be the solution of the Navier–Stokes equation at the fine level

$$\left(\rho\frac{\partial \mathbf{u}^f}{\partial t}, \mathbf{v}^f\right) + c(\rho, \mathbf{u}^f, \mathbf{u}^f, \mathbf{v}^f) + b(p^f, \mathbf{v}^f) + a(\mu, \mathbf{u}^f, \mathbf{v}^f) = (\mathbf{F}, \mathbf{v}^f) + (\mathbf{F}_s^f, \mathbf{v}^f). \tag{22}$$

Now we substitute the solution $(p^c, \mathbf{u}^c)$ of the coarse grid in (22)

$$\left(\rho\frac{\partial \mathbf{u}^c}{\partial t}, \mathbf{v}^f\right) + c(\rho, \mathbf{u}^c, \mathbf{u}^c, \mathbf{v}^f) + b(p^c, \mathbf{v}^f) + a(\mu, \mathbf{u}^c, \mathbf{v}^f) = (\mathbf{F}, \mathbf{v}^f) + (\mathbf{F}_s^f, \mathbf{v}^f) + (P^{fc}(p^c, p^f, \mathbf{u}^c, \mathbf{u}^f), \mathbf{v}^f) + (T^{fc}(\mathbf{u}^c, \mathbf{u}^f), \mathbf{v}^f), \tag{23}$$

where the fine-to-coarse momentum transfer operator P^{fc} is defined by

$$\begin{aligned}(P^{fc}(p^c, p^f, \mathbf{u}^c, \mathbf{u}^f), \mathbf{v}^f) = {} & \left(\rho\frac{\partial \mathbf{u}^c}{\partial t}, \mathbf{v}^f\right) + b(p^c, \mathbf{v}^f) + a(\mu, \mathbf{u}^c, \mathbf{v}^f) - c(\rho, \mathbf{u}^c - \mathbf{u}^f, \mathbf{u}^c - \mathbf{u}^f, \mathbf{v}^f) - \left(\rho\frac{\partial \mathbf{u}^f}{\partial t}, \mathbf{v}^f\right) \\ & - b(p^f, \mathbf{v}^f) - a(\mu, \mathbf{u}^f, \mathbf{v}^f)\end{aligned} \tag{24}$$

and the fine-to-coarse turbulent transfer operator T^{fc} by

$$(T^{fc}(\mathbf{u}^c, \mathbf{u}^f), \mathbf{v}^f) = c(\rho, \mathbf{u}^c - \mathbf{u}^f, \mathbf{u}^c - \mathbf{u}^f, \mathbf{v}^f) + c(\rho, \mathbf{u}^c, \mathbf{u}^c, \mathbf{v}^f) - c(\rho, \mathbf{u}^f, \mathbf{u}^f, \mathbf{v}^f). \tag{25}$$

The momentum transfer operator P^{fc} defines the difference between the rate of virtual work in the fine and in the coarse scale, while the turbulent transfer operator T^{fc} gives the nonlinear contribution from the fine to the coarse level.

Since the coarse scale is defined by a set of solutions in $\mathbf{X}^c(\Omega)$, $S^c(\Omega)$ we must write Eq. (23) with the test functions $\mathbf{v}^c$ in $\mathbf{X}^c(\Omega)$. We assume that the finite element space on the fine and coarse grid are embedded, namely $\mathbf{X}^c(\Omega) \subset \mathbf{X}^f(\Omega)$. This implies that any test function $\mathbf{v}^c$ can be written as a linear combination of the test functions $\mathbf{v}^f$, then

$$\left(\rho\frac{\partial \mathbf{u}^c}{\partial t}, \mathbf{v}^c\right) + c(\rho, \mathbf{u}^c, \mathbf{u}^c, \mathbf{v}^c) + b(p^c, \mathbf{v}^c) + a(\mu, \mathbf{u}^c, \mathbf{v}^c) = (\mathbf{F}, \mathbf{v}^c) + (\mathbf{F}_s^f, \mathbf{v}^c) + (S^{fc}(p^c, p^f, \mathbf{u}^c, \mathbf{u}^c), \mathbf{v}^c), \tag{26}$$

where the operator S^{fc}, which is a function only of the velocity and pressure fields over the coarse grid, is defined by

$$\begin{aligned}(S^{fc}, \mathbf{v}^f) &= (P^{fc}(p^c, p^f, \mathbf{u}^c, \mathbf{u}^f), \mathbf{v}^f) + (T^{fc}(\mathbf{u}^c, \mathbf{u}^f), \mathbf{v}^f)\\ &= \left(\rho\frac{\partial \mathbf{u}^c}{\partial t}, \mathbf{v}^f\right) + c(\rho, \mathbf{u}^c, \mathbf{u}^c, \mathbf{v}^f) + b(p^c, \mathbf{v}^f) + a(\mu, \mathbf{u}^c, \mathbf{v}^f) - (\mathbf{F}_s^f, \mathbf{v}^f) - (\mathbf{F}, \mathbf{v}^f).\end{aligned} \tag{27}$$

Eq. (27) in the multilevel approach is simply the residual of the Navier–Stokes operator at the fine level when the coarse solution is assumed to be the solution on the fine grid. It should be evident that a small value of the term S^{fc} in Eq. (26) implies that the interface is accurately resolved and that the computation of normals and curvatures over even finer grids cannot affect further the velocity and pressure fields on the coarse mesh. Clearly, the optimal situation is when $S^{fc} \approx 0$ which implies that the fine grid yields a well-resolved interface for an accurate evaluation of the capillary force. If this is not true then the operator S^{fc} must be computed directly from (27) and projected over the coarse grid to return the source term in (26). Alternatively, T^{fc} and P^{fc} could be modeled separately as two additional terms in the momentum equation at the coarse level. In the multilevel approach we are evolving the interface on a fine grid and then projecting the capillary force back on the coarse grid. The projection to the coarse level, which is basically an integration, may become quickly rather insensitive to high frequency fluctuations that may appear as we increase the number of refinement levels. The fine level is used only for a smoother description of the interface, while the relevant physics scales should be resolved at the coarse level in a satisfactory way. In this paper we consider physical situations and mesh grids where S^{fc} is approximatively zero and compute S^{fc} in a few instances only to evaluate the error of this assumption.

Similarly, if we introduce the coarse velocity field $\mathbf{u}^c$ in the advection equation for χ integrated on the mesh at the fine level, see Eqs. (17) and (18), we get

$$\int_\Omega \frac{\partial \chi}{\partial t}\varphi_i^f\, dV + \int_{\Gamma_i^f} \chi(\mathbf{u}^c \cdot \mathbf{n})\varphi_i^f\, dS = \int_\Omega V^{fc}(\mathbf{u}^c, \mathbf{u}^f)\varphi_i^f\, dV, \tag{28}$$

where V^{fc} is the fine-to-coarse color function transfer operator. The term

$$\int_\Omega V^{fc}(\mathbf{u}^c, \mathbf{u}^f)\varphi_i^f\, dV = \int_{\Gamma_i^f} ((\mathbf{u}^c - \mathbf{u}^f) \cdot \mathbf{n})\varphi_i^f\, dS \tag{29}$$

represents the error in volume/area due to the use of a velocity field over the fine mesh which is not divergence-free. This error is again due to the projection of the coarse velocity field to the fine level (f) and can be removed in different ways, for example with a local redistribution algorithm [31,33]. In the simulations presented in this paper, the volume/area error is usually very small and is simply ignored.

3. Numerical implementation

3.1. Dimensionless multilevel equations

In order to solve the Navier–Stokes system (16) we use the following nondimensional variables

$$\mathbf{x}^* = \frac{\mathbf{x}}{D}, \quad t^* = \frac{tD}{U}, \quad \mathbf{u}^* = \frac{\mathbf{u}}{U}, \quad p^* = \frac{p}{\rho_l U^2}, \quad \rho^* = \frac{\rho}{\rho_l}, \quad \mu^* = \frac{\mu}{\mu_l}, \quad \sigma^* = \frac{\sigma}{\sigma_r},$$

where D is the jet diameter, $U = |u_l - u_g|$ the relative velocity of the jet at the inlet and σ_r the surface tension coefficient of the liquid/gas interface. In the rest of the paper we drop the star superscript in the dimensionless quantities and use the standard definition of the Reynolds, Weber and Froude numbers

$$Re = \frac{\rho_l U D}{\mu_l}; \quad We = \frac{\rho_l U^2 D}{\sigma_r}; \quad Fr = \frac{U^2}{|\mathbf{g}|D}. \tag{30}$$

Furthermore, $Ca = We/Re$, $Bo = We/Fr$ and $Oh = \sqrt{Ca/Re}$ are the capillary, Bond and Ohnesorge numbers, respectively. The final dimensionless system consists of a set of two equations at the coarse level (c)

$$\left(\rho^c\frac{\partial \mathbf{u}^c}{\partial t}, \mathbf{v}^c\right) + c(\rho^c, \mathbf{u}^c, \mathbf{u}^c, \mathbf{v}^c) - b(p^c, \mathbf{v}^c) + \frac{1}{Re}a(\mu^c, \mathbf{u}^c, \mathbf{v}^c) = \frac{1}{Fr}(\rho^c \mathbf{g}, \mathbf{v}^c) + \frac{1}{We}(\mathbf{F}_s^f, \mathbf{v}^c), \quad b(q^c, \mathbf{v}^c) = 0 \tag{31}$$

and the advection equation for the color function at the fine level (f)

$$\int_{\Omega} \frac{\partial \chi}{\partial t} \varphi_i^f \, dV + \int_{\Gamma_i^f} (\hat{\mathbf{u}}^f \cdot \mathbf{n}) \varphi_i^f \, dS = 0, \tag{32}$$

where $\hat{\mathbf{u}}^f$ is the projection on the fine level of the nondimensional velocity $\mathbf{u}^c$ of the coarse level. The density is defined in each cell of the coarse mesh by $\rho^c = \rho_l C^c + \rho_g(1 - C^c)$ and similarly the viscosity. The color function C^c is computed as the average of the color functions at the fine level in the same coarse cell. In this paper we assume that the mesh resolution is high enough so that the terms P^{fc}, T^{fc} and V^{fc} are all negligible.

3.2. Numerical implementation of the multilevel VOF method

The multilevel VOF method advances in time on a Cartesian grid the C data at the fine level (f) by integrating (32) and then projects the resulting color function C^f and the surface tension force $\mathbf{F}_s^f$ on the coarse level (c) where the pressure and velocity fields are computed. Each additional level of grid refinement roughly doubles the number of mixed cells; but even with several extra refinement levels, the volume tracking overhead is small, compared to the rest of the calculation.

However, it would require a considerable amount of memory space to store the full matrix of the C^f data, in particular for three-dimensional computations. Since the spatial distribution of the C field changes in time, all the entries of the color function matrix must be available and this requires also the storage of empty and full cells which may become mixed cells at some later time in the simulation.

In this paper we propose a multilevel storage scheme which memorizes the whole matrix of the color function at the coarse level (c), so that density and viscosity can be computed at this level, but only sparse data at the fine level (f), implementing in this way the storage of the interface data alone at each time step. This allows us to compute the color function distribution over a highly-refined mesh with an accuracy and efficiency comparable to an adaptive mesh refinement method. The format is similar to the Compressed Row Storage (CRS) [34]. We illustrate this technique in two dimensions in Fig. 2 by considering a 5×5 Cartesian mesh with the corresponding C data. The extension to three dimensions is straightforward. For each row we store the number of entries n_c, the C data and their column number. Notice that empty cells are not stored, while a sequence of n consecutive full cells is stored as a single one, with its color function value equal to n in the first internal cell position. For example in the third row of Fig. 2 we have three consecutive full cells, hence $C = 3$, with the first one in the second column. With this technique we can describe interfaces on a very refined mesh while the storage requirements are proportional to the length of the interface divided by the fine grid spacing. This representation requires an efficient numerical algorithm to extract and compress the data in the compact sparse matrix representation. In Fig. 3 we show the full color function matrix at the coarse level (c) with 24×16 cells, and the sparse color function matrices at the two levels $f = c + 2$ and $f = c + 4$. At the intermediate level of refinement each cell of the coarse grid is divided in 16 subcells with the interface clearly marked on the grid. At the highest level of refinement each coarse cell is subdivided into 256 smaller cells,

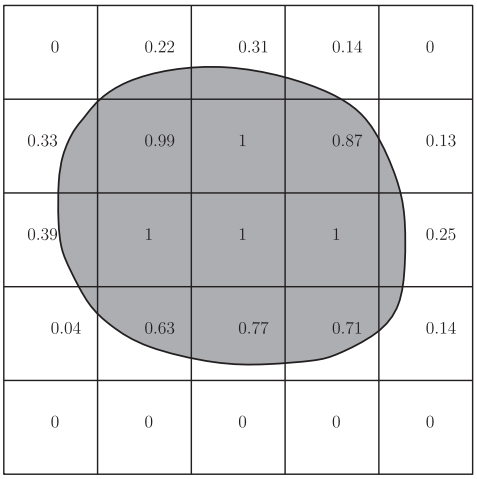

row	n_c	C					column				
1	3	0.22	0.31	0.14			2	3	4		
2	5	0.33	0.99	1	0.87	0.13	1	2	3	4	5
3	3	0.39	3	0.25			1	2	5		
4	5	0.04	0.63	0.77	0.71	0.14	1	2	3	4	5
5	0										

Fig. 2. The C data distribution on a 5×5 Cartesian mesh (top) and the stored data (bottom), including the row number, the number of cells n_c, the color function in the mixed and consecutive full cells and the column position.

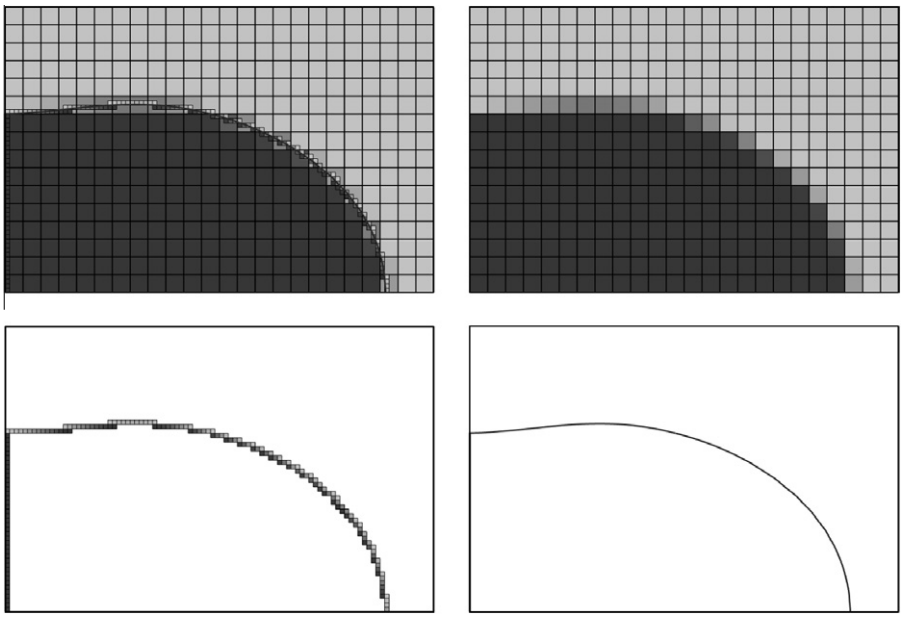

Fig. 3. The color function distribution on different meshes (top left) and on the coarse mesh (top right). The compact data memorization with two (bottom left) and four (bottom right) levels of grid refinement.

with matrix entries about 16 times those of the coarse grid. The VOF interface at this level is very close to a front tracking representation with markers.

The dynamics is computed at the coarse level while the fine grid is used to approximate the interface and calculate the capillary forces. We consider a Piecewise Linear Interface Calculation (VOF/PLIC), that includes the calculation of the reference phase fluxes across the cell boundary to update the C data at the next time step. In the reconstruction step the interface is approximated in each mixed cell by a single segment. The normal vector to this segment is computed with the ELVIRA algorithm which finds the best linear approximation of the interface among a set of six candidates, obtained by using the color function values on a 3×3 block of cells and centered, forward and backward difference schemes for the first derivative. Each segment is extended to the block, defining a tentative volume fraction value in each cell of the block, and the selected candidate is the one that minimizes the error between the tentative and the actual values [3,31,35,36]. However due to the compact representation of the color function, it is not very efficient to extract the block of C data whenever we change the cell under investigation. For this reason, we have implemented a fast data extraction/compression algorithm that computes the normals in all the cells of a given row j, by storing also the C data of the rows $j-1$ and $j+1$ in a temporary $N \times 3$ portion of the full matrix. We then substitute the data in the row $j-1$ with those of row $j+2$ and reconstruct the normal for the mixed cells of row $j+1$.

In the advection step we solve the discrete version of (32) written for the color function C_i^f

$$C_i^f(t+\Delta t) = C_i^f(t) + \sum_{k=1}^{4} \Phi_{i,k}(\chi, \hat{\mathbf{u}}^f, \mathbf{n}), \tag{33}$$

where i is the cell index, k the index over the cell sides. We use a geometric unsplit area-preserving advection method to compute the cell boundary fluxes $\Phi_{i,k}$ [36,3], which requires the projected velocity $\hat{\mathbf{u}}^f$, the phase indicator χ and the normal vector $\mathbf{n}$ computed in the reconstruction step. The matrices containing the two normal components are compressed exactly in the same way as the C data.

3.3. Numerical implementation of the capillary force

In jet dynamics the numerical implementation of the capillary force must be sufficiently accurate. In this paper the surface tension force is computed at the fine level (f) starting from (12)

$$(\mathbf{F}_s^f, \mathbf{v}^c) = \int_{\Gamma_s} \sigma\kappa\mathbf{n} \cdot \mathbf{v}^c \, dS, \tag{34}$$

where we have introduced the curvature $\kappa = \kappa_1 + \kappa_2$, with κ_1 and κ_2 the principal curvatures in axisymmetric geometry with cylindrical coordinates r, ϕ, and z. We can easily compute in this geometry the curvature of the interface Γ_s, given by the revolution around the z-axis of the interface line L_s of equation $r = f(z)$. Each meridian plane through the z-axis contains the line L_s and is also perpendicular to the local tangent plane in each point of Γ_s. The local curvature κ_1 on L_s is given by

$$\kappa_1 = \frac{f''(z)}{(1+f'^2(z))^{3/2}}. \tag{35}$$

The other curvature κ_2 is computed on a third plane that is perpendicular to both the tangent and the meridian planes and that contains the local normal vector to the line L_s. If we denote with φ the angle between the outgoing normal vector and the z-axis, then

$$\kappa_2 = -\frac{\cos\varphi}{r} = -\frac{1}{f(z)(1+f'^2(z))}. \tag{36}$$

The surface force (34) is rewritten as

$$(\mathbf{F}_s^f, \mathbf{v}^c) = \int_{\Gamma_s} \sigma\kappa_1 \mathbf{n}\cdot\mathbf{v}^c\, dS + \int_{\Gamma_s} \sigma\kappa_2 \mathbf{n}\cdot\mathbf{v}^c\, dS \tag{37}$$

where $\kappa_2 = -\cos\varphi/r$ is known analytically and the computation of the curvature κ_1 is performed by the introduction of the two-dimensional Laplace–Beltrami operator.

In the FEM variational formulation, the computation of the curvature with the Laplace–Beltrami operator requires only the interface position and its computation can be embedded, even implicitly, in the Navier–Stokes solver. In axisymmetric geometry this operator acts only on the interface line L_s and can be written as

$$\frac{d}{ds} = (I - \mathbf{nn})\cdot\nabla \tag{38}$$

with ∇ the two-dimensional gradient operator in the coordinates r and z. Integrating by parts the first term on the r.h.s. of (37) we obtain

$$\int_{L_s} \sigma\kappa_1 \mathbf{n}\cdot\mathbf{v}^c\, d\ell = \sigma\int_{L_s} \frac{d^2}{ds^2}\mathbf{x}_s\cdot\mathbf{v}^c\, d\ell = -\sigma\int_{L_s} \frac{d}{ds}\mathbf{x}_s\cdot\frac{d}{ds}\mathbf{v}^c\, d\ell. \tag{39}$$

An extensive mathematical analysis of the Laplace–Beltrami operator for curvature computations in two-phase flow can be found in [24,37–40]. The mathematical proof of convergence can be found in [37] and an extensive study of spurious currents for a static droplet is performed in [38] for different finite elements and in particular for Taylor–Hood elements. Spurious current tests with our code return similar rates. The implicit implementation of the tension surface term is in [40] and an extended new finite element for pressure discontinuities in two-phase flow is proposed in [39].

The interface instabilities depend on small pressure perturbations and an accurate computation of the pressure around the interface is an important issue. In jet dynamics, interface instabilities may be artificially excited or affected by the presence of spurious currents, which are unphysical flows generated near an interface where locally the pressure and capillary forces are not well balanced numerically. Since our goal is to measure the growth rate of the physical instability accurately, we must eliminate the spurious currents which are present in the static cylindrical solution. In this configuration κ_1 is zero and only the surface tension term with curvature κ_2 produces spurious currents.

A few schemes have been proposed to compensate the pressure term and provide an accurate surface tension representation in the static case when the curvature is known. Among them we can mention the balanced-force method, described in [23,14], for Navier–Stokes solvers based on the pressure-projection method or the pressure volumetric compensation methods described in [24,25,41]. These methods are somewhat similar since they both rely on a consistent discretization and balance of the forces on the boundary of the cell. For the term containing the curvature κ_2 we consider a volumetric approach. The convergence analysis and numerical implementation of the volumetric approach for a droplet in static equilibrium and its dynamic oscillations can be found in [24,25], where the interface is a continuous chain of segments. In this paper the chain is discontinuous, but this feature is mitigated by the fact that with the multilevel VOF approach we have more segments in each cell of the coarse mesh than in the continuous case.

The volumetric approach is based on the divergence theorem, so we write

$$\int_{\Gamma_s} \sigma\kappa_2\mathbf{v}^c\cdot\mathbf{n}\, dS = \int_{\Omega_l} \sigma\nabla\cdot(\hat{\kappa}_2\mathbf{v}^c)\, dV = \int_{\Omega} \chi\sigma\nabla\cdot(\hat{\kappa}_2\mathbf{v}^c)\, dV = \int_{\Omega} \chi\sigma\hat{\kappa}_2\nabla\cdot\mathbf{v}^c dV + \int_{\Omega} \chi\sigma\mathbf{v}^c\cdot\nabla\hat{\kappa}_2\, dV. \tag{40}$$

In (40) $\hat{\kappa}_2$ can be any extension of κ_2 over Ω as long as $\hat{\kappa}_2$ matches κ_2 on the interface Γ_s. If χ, which is discontinous on Γ_s, is approximated by the discrete values $\hat{\chi}_h$ on the cell vertices, then the surface tension term becomes

$$\int_{\Gamma_s} \sigma\kappa_2\mathbf{v}^c\cdot\mathbf{n}\, dS = \int_{\Omega} \hat{\chi}_h\sigma\hat{\kappa}_2\nabla\cdot\mathbf{v}^c\, dV + \int_{\Omega} \hat{\chi}_h\sigma\mathbf{v}^c\cdot\nabla\hat{\kappa}_2\, dV. \tag{41}$$

Notice that for an equilibrium configuration the first term balances the pressure jump at the interface while the second term is the source of the spurious currents. Through the extension $\hat{\kappa}_2$ and the $\hat{\chi}_h$ we transport the forces from the interface inside the cell to the cell sides, obtaining in this way the desired compensation of the pressure. The extension $\hat{\kappa}_2$ can be computed in many ways, however, in the static case, the extended curvature $\hat{\kappa}_2$ must match the constant value of κ_2. In particular, in

the cylindrical configuration we compute the value of κ_2 on the interface at any z and then extend it uniformly in the radial direction. The Navier–Stokes equation becomes

$$c(\rho,\mathbf{u},\mathbf{u},\mathbf{v}) + b(p,\mathbf{v}) + a(\mu,\mathbf{u},\mathbf{v}) = b(\hat{\chi}_h\sigma\hat{\kappa}_2,\mathbf{v}) + (\hat{\chi}_h\sigma\nabla\hat{\kappa}_2,\mathbf{v}^c), \tag{42}$$

which gives exactly the equilibrium solution $p = \chi_h\sigma\hat{\kappa}_2$ and $\mathbf{u} = 0$ with no spurious currents if the pressure and χ_h are defined over the same finite dimensional space S_h.

4. Numerical tests

4.1. Linear dispersion equation for jets

As a first test we consider the evolution of small perturbations of an axisymmetric jet, when nonlinear effects are still negligible. For a correct description of the phenomenon spurious currents must be negligible, since the surface tension term plays a key role in the numerical evaluation of the dispersion equation that relates the growth rate of the instability to the physical and geometrical parameters of the liquid jet. An analytical dispersion equation was derived in [42], where it was shown that asymmetric modes can be excited when the Weber number is greater than a critical value We_c. This value is a function of the wavelength of the disturbance and the density ratio between the gas and liquid phases. In this paper we perform only axisymmetric simulations, then We must be smaller than We_c. We recall briefly the dispersion relation following the derivation in [42], which considers the stability of a wave of very small amplitude on a cylindrical jet of infinite length. The liquid jet with density ρ_l and radius R has a uniform relative velocity U with respect to the external gas with density ρ_g. The two fluids are assumed to be incompressible and inviscid. If the system is subject to a small disturbance, the expressions for the linear perturbed quantities are

$$p'_j(r,\theta,z,t) = p_j(r)exp(i(kz + m\theta) + \alpha t), \tag{43}$$

$$\mathbf{u}'_j(r,\theta,z,t) = \mathbf{u}_j(r)exp(i(kx + m\theta) + \alpha t), \tag{44}$$

where $j = l, g$ and α is the complex growth rate with respect to time. For the azimuthal mode $m = 0$, also known as varicose or sausage mode, the cross section of the jet is circular and its radius varies only with the z-coordinate. When $m > 0$ the modes are asymmetric. For the mode $m = 1$ the cross section of the jet is still circular but the axis of the perturbed jet describes a spiral around the z-axis. This is usually named *snake* or *kink* mode. For $m = 2$, the cross section of the jet is elliptic, and an originally circular jet deforms progressively into a flat curling sheet. For larger m values, the modes are characterized by m oscillations along the unperturbed circumference.

The analysis of the dispersion relation for the perturbations (43) and (44) in the presence of an external fluid phase shows that surface tension has a stabilizing effect on asymmetric modes that can only develop for sufficiently large Weber numbers. The critical Weber number $(We_c)_m$ is defined as the Weber number over which the growth rate of the mth mode is greater than zero. For an inviscid jet the following relation has been derived [42]

$$(We_c)_m = \frac{(\gamma_m + q\beta_m)[m^2 + (kR)^2 - 1]}{kRq\gamma_m\beta_m} \tag{45}$$

with

$$\gamma_m = k\frac{I_m(kR)}{I'_m(kR)}, \quad \beta_m = -k\frac{K_m(kR)}{K'_m(kR)}, \tag{46}$$

where I_m and K_m are the mth order modified Bessel functions of the first and second kind, I'_m and K'_m their first derivative and $q = \rho_g/\rho_l$. In the limit of both short and long wavelengths the first asymmetric mode to be excited is the $m = 1$ mode. More particularly, with a long wavelength disturbance the $m = 1$ mode grows when $We > (1 + q)/q$, and for a short wavelength when $We > ((1 + q)k\ R)/q$. The critical Weber number We_c is always proportional to the inverse of the density ratio q and as $q \to 0$ then $We_c \to \infty$, in agreement with Rayleigh's theory [43], and the mode is always axisymmetric. If $q = 1.3 \times 10^{-3}$, as in an air/water system, the lowest critical Weber number is $We_c \approx 769$, and $m = 1$.

Below this critical value only the $m = 0$ mode is present and the growth rate α is the solution of the following characteristic equation [42]

$$(\rho_l\gamma_0 + \rho_g\beta_0)\alpha^2 + 2ik\alpha(\rho_g\beta_0 u_g + \rho_l\gamma_0 u_l) - k^2\left(\rho_g\beta_0 u_g^2 + \rho_l\gamma_0 u_l^2\right) - k\frac{\sigma}{R^2}[1 - (kR)^2] = 0. \tag{47}$$

If we set $\alpha = \alpha_r + i\alpha_i$ in the previous quadratic equation then the real part of the roots is given by

$$\alpha_r = \pm\frac{U}{R}\sqrt{\frac{\gamma_0\beta_0 q(kR)^2}{(\gamma_0 + \beta_0 q)^2} + \frac{1}{We}\frac{(kR)[1 - (kR)^2]}{(\gamma_0 + \beta_0 q)}}, \tag{48}$$

with $We = (RU^2\rho_l)/\sigma$.

There are three interesting cases of (48). The first is the Rayleigh equation for a liquid jet in the vacuum obtained as q approaches zero

$$\alpha_r = \pm\frac{U}{R}\sqrt{\frac{1}{We}\frac{(kR)[1-(kR)^2]}{\gamma_0}}. \tag{49}$$

The short wavelength limit is obtained for $kR \to \infty$ and $\beta_0 = \gamma_0 = 1$

$$\alpha_r = \pm\frac{U}{R}\sqrt{\frac{(kR)^2 q}{(1+q)^2}+\frac{1}{We}\frac{(kR)[1-(kR)^2]}{1+q}}. \tag{50}$$

Finally, the long wavelength limit has $k = 2\pi R/\lambda \to 0$, $\beta_0 \to -kRln(kR)$ and $\gamma_0 \to 2/(kR)$, then

$$\alpha_r = \pm\frac{U}{R}\sqrt{-\frac{2(kR)^3 ln(kR) q}{[2-q(kR)^2 ln(kR)]^2}+\frac{1}{We}\frac{(kR)^2[1-(kR)^2]}{[2-q(kR)^2 ln(kR)]}}. \tag{51}$$

Eq. (51) shows that the larger the Weber number the more stable the liquid jet to axisymmetric perturbations of long wavelength. In order to reproduce the analytical result of (49) we consider the cylindrical domain shown in Fig. 4. A liquid of density ρ_l and viscosity μ_l is located within a cylindrical region Ω_l of radius R. The liquid is surrounded by a gas of density ρ_g and viscosity μ_g. We assume periodic boundary conditions on the two bases of the cylinder and free flow conditions on its lateral surface. The initial velocity field in both fluids is zero and the position r_I of the interface is perturbed in the form

$$r_I = r_I(z) = R + \delta_0 \cos\left(\frac{2\pi z}{\lambda}\right), \tag{52}$$

where δ_0 is the initial amplitude and λ the wavelength of the perturbation.

In order to compute the growth rate we need to use very small values of δ_0 and of the velocity field. If the capillary force (34) is not carefully discretized, for δ_0 that goes to zero and with a small initial velocity, the motion could be dominated by the spurious currents. Since δ_0 can be chosen very small so that $\kappa_1 \simeq 0$, then the spurious currents at the initial time can be generated only by the surface tension term containing the curvature κ_2. With the volumetric approach given by (41) the spurious currents are indeed negligible and the pressure jump is correctly reproduced.

To compute the growth rate we use the linearized version of (26) to evolve in time the velocity and pressure fields. The procedure is divided in two steps as shown in Fig. 5. In the first step, we start at time $t = 0$ with the velocity and pressure profiles of the steady-state solution but with the perturbed interface of (52) and evolve the system with very small time

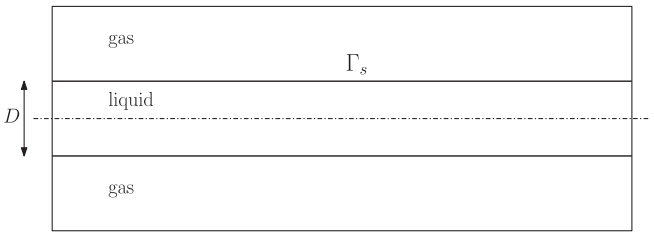

Fig. 4. Initial axisymmetric geometry.

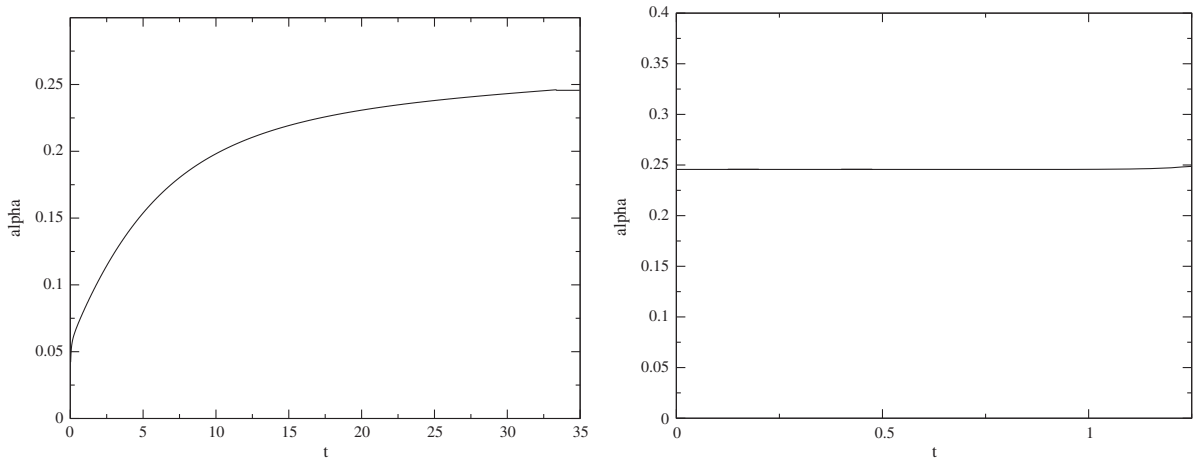

Fig. 5. Time evolution of the growth rate α_r for the $m = 0$ mode during the initial transient (left) and after the restart of the computation (right).

steps. When the growth rate α_r approaches a stationary value, the velocity and pressure fields are then consistent with the perturbed interface and we assume these profiles as the initial configuration for the second part of the simulation. We then monitor the time evolution of the value of α_r that should remain about constant, as shown on the right of Fig. 5.

In Fig. 6 we plot the dispersion relation of the growth rate α_r as a function of the nondimensional wave number kR, for different resolutions of the coarse mesh and different levels of refinement. The radius of the liquid cylinder is $R = 0.328125 \times 10^{-3}$ m with a perturbation amplitude $\delta_0 = 0.01R$. The fluid density is $\rho_l = 1000\ \mathrm{kg/m^3}$, its viscosity $\mu_l = 0.0316$ kg/ms and the surface tension coefficient $\sigma = 0.0725\ \mathrm{J/m^2}$. The density ratio is $\rho_l/\rho_g = 1000$, and the viscosity ratio $\mu_l/\mu_g = 100$. For these physical parameters, the nondimensional numbers are $Re = 10.38$, $We = 4.53$ and $Oh = 0.205$, with the reference velocity computed as $U = \sqrt{\sigma\kappa_2/\rho_l}$. The curves on the left are obtained with 32, 64, 128 cells in the radial direction with two refinement levels for the color function, $f = c + 2$. The curves on the right consider 64 cells in the radial direction and 2, 3, 4 refinement levels. In the two graphs we also plot the inviscid theoretical curve of (49). We observe that for this test the numerical results are slightly different only at the lowest resolution with 32 cells, while they are rather insensitive to the number of refinement levels.

In Fig. 7 we show how the dispersion relation of the growth rate changes with the viscosity ratio μ_l/μ_g for the three values 10, 100, 1000. Since the density ratio is rather high, the results are already close to the asymptotic line at moderate viscosity ratios, $\mu_l/\mu_g \approx 100$.

Finally, in Fig. 8 we compute the dispersion relation of the growth rate by varying the viscosity μ_l of the liquid phase. In the first graph the physical parameters are those of Fig. 6, in the second case the liquid viscosity is changed, $\mu_l = 0.01$ kg/ms then $Oh = 0.065$, but the viscosity ratio remains the same. The continuous lines in Fig. 8 represent the dispersion relation from the linear stability analysis of a viscous liquid jet surrounded by the vacuum, $\rho_g = \mu_g = 0$, derived by Weber [44]. These results should be compared with those obtained in [5] with a coupled level set/VOF/ghost fluid method that progressively underestimates the growth rate as the wave number increases. The general agreement with the theoretical dispersion relation does not change as we decrease by an order of magnitude the liquid viscosity, i.e. $\mu_l = 0.0031$, 0.001.

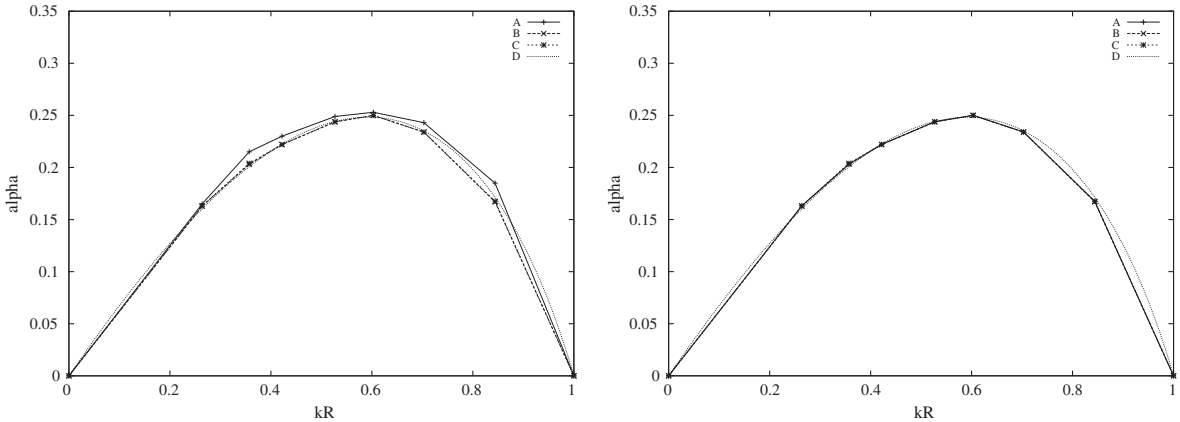

Fig. 6. Dispersion results for $\mu_l/\mu_g = 100$ for different mesh resolutions on the left (32 (A), 64 (B), 128 (C)) and for a different number of refinement levels on the right ($f = c + 2$ (A), $f = c + 3$ (B), $f = c + 4$ (C)). In both graphs it is also plotted the inviscid theoretical curve of (49) (D).

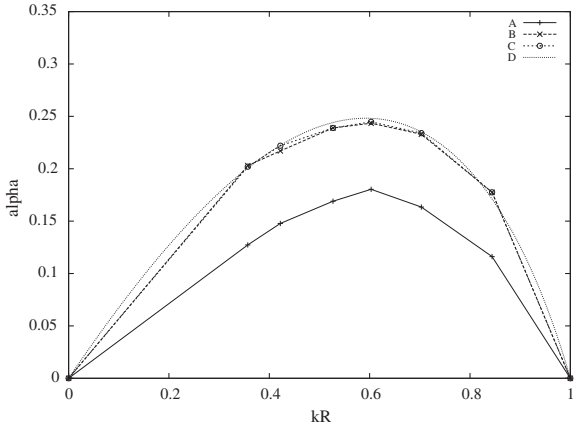

Fig. 7. Numerical growth rate α for different viscosity ratios μ_l/μ_g (10 (A), 100 (B) and 1000 (C)). In the graph it is also plotted the inviscid theoretical curve of (49) (D).

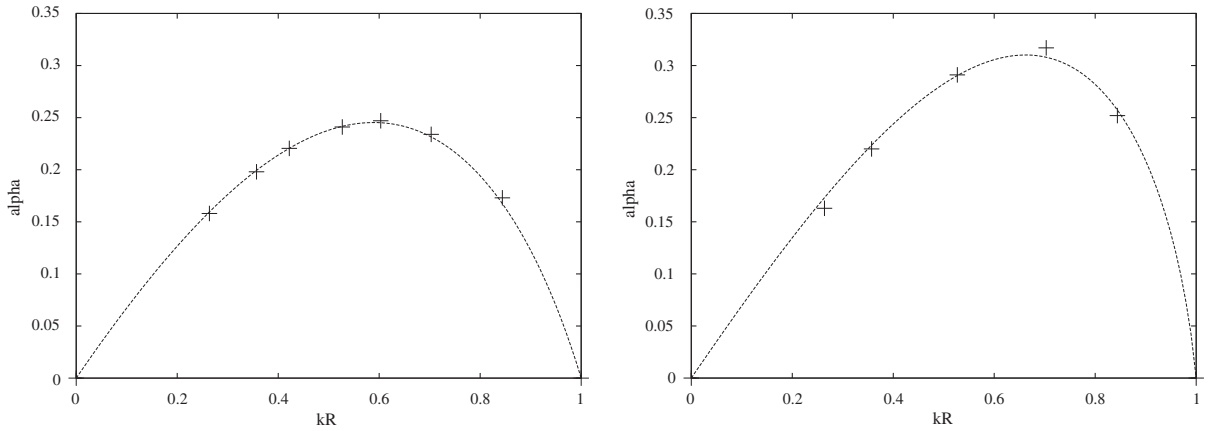

Fig. 8. Numerical (+) and theoretical dispersion for the growth rate for $Oh = 0.205$ (left) and $Oh = 0.065$ (right).

4.2. Axisymmetric pulsating jets

The evolution of a liquid jet exiting a nozzle is strongly influenced by the interaction with the surrounding gas. This phenomenon has been studied extensively theoretically, numerically and experimentally [45]. However a real jet cannot be easily reproduced, since the instabilities of the process are initiated by small perturbations which are generated at the inlet and

Table 1
The maximum value of $\|S_c^{fc}\|_\infty / \|\mathbf{F}_s\|_\infty$ for the coarse grid with 32×192 cells, four different refinement levels, in the nondimensional time interval [0,2].

level	1	2	3	4
Cells	64×384	128×768	256×1536	512×3072
Error	8.2×10^{-2}	1.2×10^{-2}	5.1×10^{-4}	7.1×10^{-4}

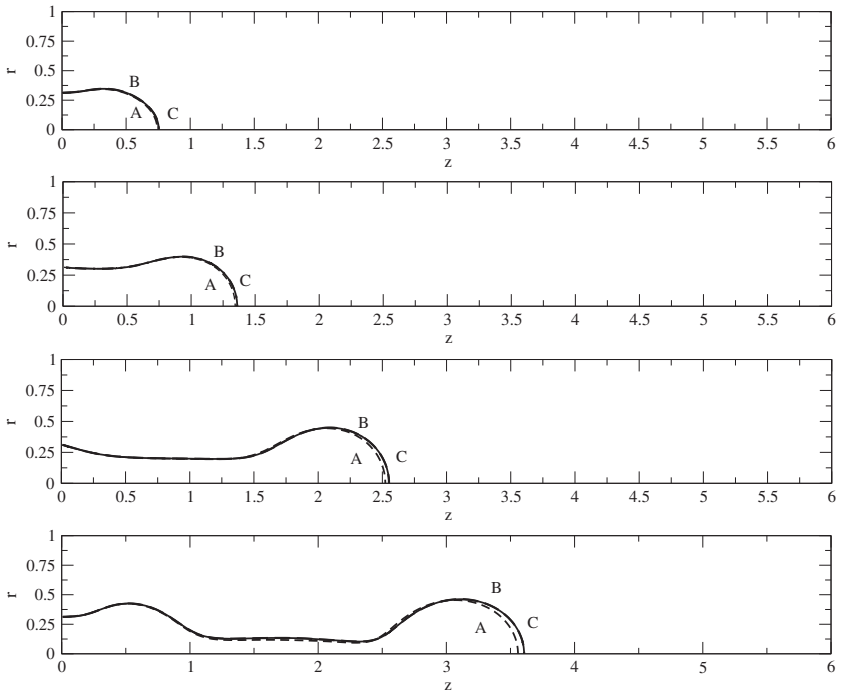

Fig. 9. Evolution of the interface line for the three different grid resolutions: 32×192 (A), 64×384 (B) and 128×768 (C), at the nondimensional times $t = 0.5, 1, 2, 3$.

also upstream in the bulk of the jet. These perturbations are mostly of stochastic nature, related to turbulence and it is not easy to quantify them. The aim of this section is to study the evolution of jets with a sinusoidal oscillation superposed to a constant injection velocity that allows the observation of some elementary and well-defined effects such as a the breakup of the whole column and the formation of single droplets and threads. Thus we consider the following expression of the inlet velocity of the liquid jet flowing into a stationary gas

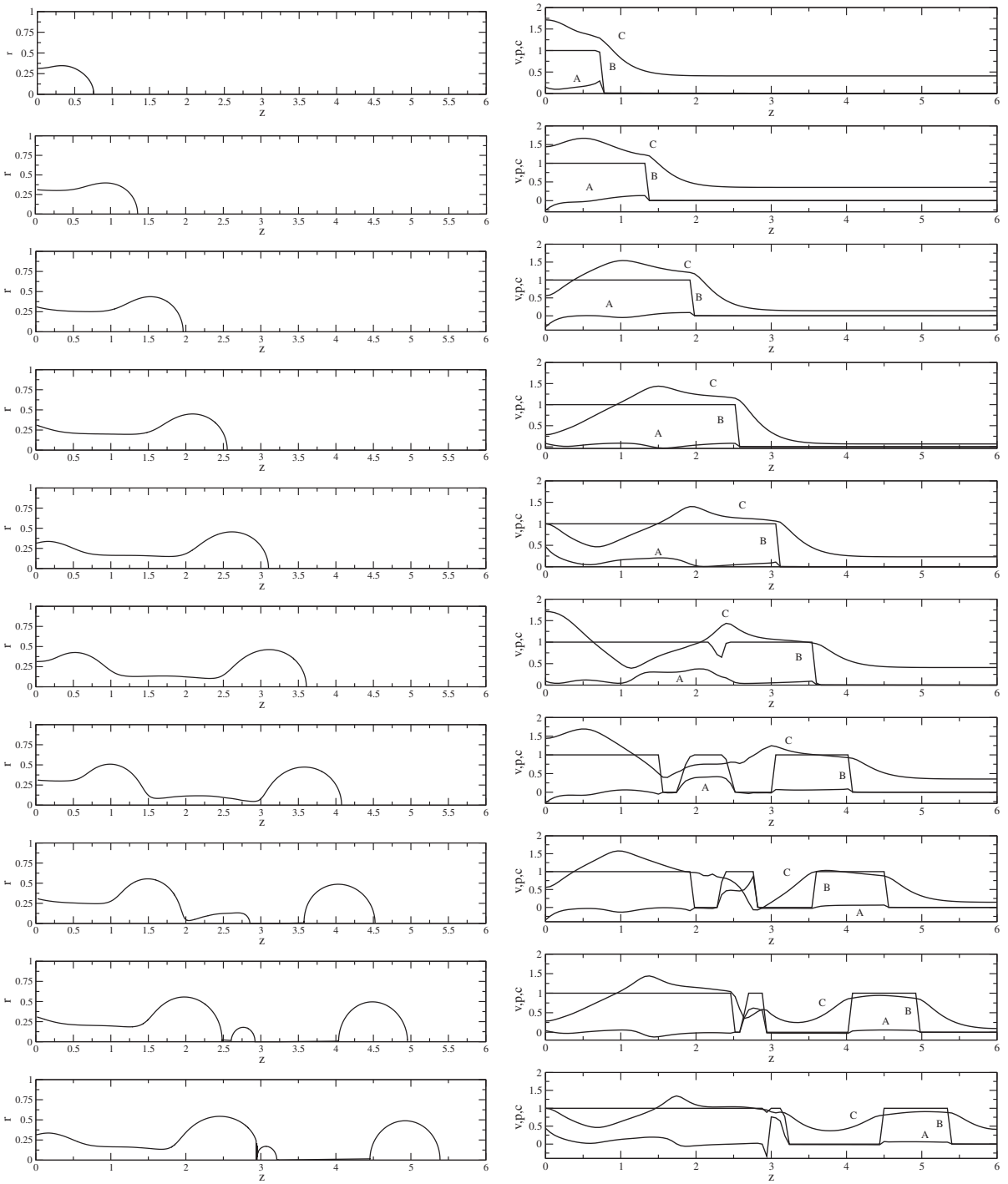

Fig. 10. Interface evolution (left) and pressure, color function and velocity profiles along the jet axis (right, lines A, B and C, respectively) at times 0.5, 1, 1.5, 2, 2.5, 3, 3.5, 4, 4.5, 5 (top to bottom).

$$U = U_0(1 + A\sin(\omega t)) \tag{53}$$

with $\omega k = U_0$. Since we are interested in jets with a small diameter the gravity term can be neglected and the Froude number is assumed to be infinite. We are left with four dimensionless parameters governing the jet decay: the driving amplitude A, the nondimensional or reduced wavenumber kR, the Weber number We and the Ohnesorge number Oh. The range of possible dynamics in this parametric space has never been fully explored. In this study we only consider three different wavelengths, around the maximum of Fig. 8, and three inlet velocity up to a Weber number greater than the critical value. We also monitor the magnitude of the transfer operator S^{fc} with respect to the capillary force term.

4.2.1. Convergence test

First we study a simple jet in order to determine a consistent set of fine and coarse meshes and verify that S^{fc} is always small during the simulation. To address this issue we consider a jet of fluid with density $\rho_l = 1000\ \mathrm{kg/m^3}$, viscosity $\mu_l = 0.003$ kg/ms and surface tension coefficient $\sigma = 0.0725\ \mathrm{J/m^2}$, injected with velocity $U_0 = 1$ m/s from a hole with radius $R = 0.3164 \times 10^{-3}$ m. In this case we have $Re = 210.93$, $We = 8.73$ and $Oh = 0.014$. The density ratio between the liquid and gas phases is again 1000 and the viscosity ratio 100. The amplitude of the sinusoidal oscillation of the inlet velocity is $A = 0.5$, its wavelength $\lambda = 3.5 \times 10^{-3}$ m, then the reduced wavenumber is $kR = 0.57$. For this set of physical parameters the critical Weber number is $We_c \approx 1000$, and the jet decay is fully axisymmetric. At the initial time the gas fills in the whole computational domain and the liquid is injected from the left boundary of Fig. 1 with the velocity defined in (53). The introduction of a pulsating source drives the formation of the droplet and allows us to analyze with great detail the breakup process in a limited domain in the axial direction ($L_z \approx 18R$).

We wish to determine a solution of the jet problem with the multilevel VOF method which is well resolved at the coarse level, Eqs. (31) and (32), with the transfer operator (27) being negligible. First we consider simulations with only one level and at different resolutions with the result that the interface, in the two meshes with 16×96 and 32×192 cells, breaks very irregularly with the formation of several small droplets. The computations produce a single stable droplet only for resolutions equal or higher than 128×768. This will be considered the lowest resolution for the fine grid.

In this multilevel test we consider a coarse grid with 32×192 cells and four levels of refinement ($f = c + l$, $l = 1, 2, 3, 4$), that are obtained with a simple midpoint rule where the number of cells in each direction doubles as we consider the next

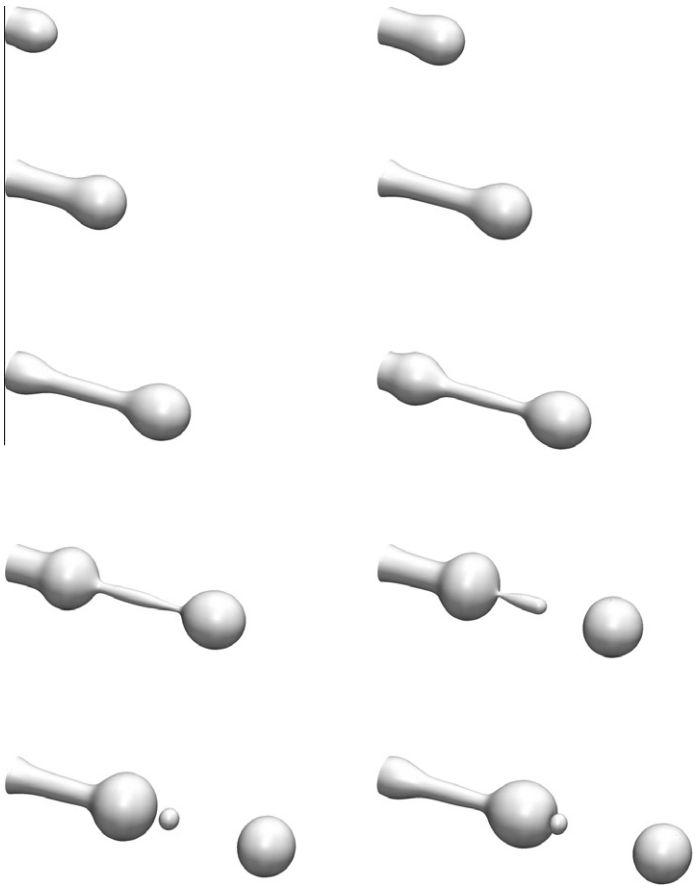

Fig. 11. Jet evolution for the intermediate wave length λ_2 at times 0.5, 1, 1.5, 2, 2.5, 3, 3.5, 4, 4.5, 5 (left to right and top to bottom).

more refined grid. The most refined fine mesh has 512×3072 cells. For $i = 1$ the interface breaks as in the single-level simulations, while for $i = 2, 3, 4$ the color function is well resolved, however the norm of the transfer operators S^{fc} in (27) is not always negligible. The postprocessing computation of the operator S_c^{fc} in the coarse grid can be performed with the projection P^{cf} and the restriction R^{fc} operators that are already used in the multigrid solver of the Navier–Stokes equations. We first compute (27) for all basis functions $\mathbf{v}_i^f$ at the fine level

$$\left(S_f^{fc}, \mathbf{v}_i^f\right) = \left(S^{fc}(P^{cf}[(\mathbf{u}^c, p^c)]), \mathbf{v}_i^f\right). \tag{54}$$

We then use the restriction operator R^{fc} to compute the projection S_c^{fc} over the coarse grid

$$\left(S_c^{fc}, \mathbf{v}_j^c\right) = R^{fc}\left[\left(S_f^{fc}, \mathbf{v}_i^f\right)\right] \tag{55}$$

for all basis functions $\mathbf{v}_j^f$ at the coarse level. In Table 1 we report the maximum value during the time interval [0,2] of the ratio between the transfer operator S^{fc} and the capillary force term. The transfer operator can be neglected for the two refinement levels $l = 3, 4$, for which the computation of the local normals and curvatures can be considered accurate for the given coarse grid.

We remark that this does not imply that the pressure and velocity fields at the coarse resolution 32×192 are fully resolved, but only that the interface representation at the two highest refinement levels is accurate for the coarse grid. In order to discuss the accuracy of the solution we consider three different coarse grids, each of them with a fine mesh with four refinement levels: case *A* with 32×192 cells, case *B* with 64×384 cells and case *C* with 128×768 cells. In Fig. 9 we show the evolution of the interface line, always computed with the nondimensional time step $\Delta t = 1 \times 10^{-3}$. The evaluation of the maximum value in the whole simulation of the ratio between the transfer operator and the capillary force gives 8.03×10^{-4} for case *A*, 3.63×10^{-5} for case *B* and 1.04×10^{-5} for case *C*. Even if this ratio is very small for all three cases the interface at the lowest resolution does not overlap precisely with the solution of the other two resolutions. The solution of cases *B* and *C*

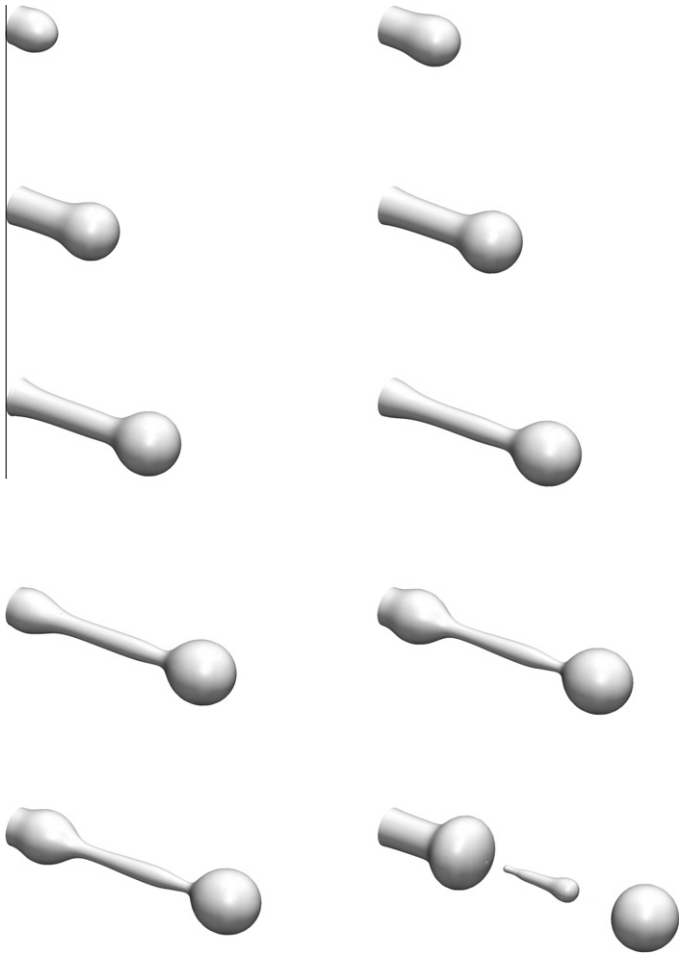

Fig. 12. Jet evolution for the shortest wave length λ_1 at times 0.5, 1, 1.5, 2, 2.5, 3, 3.5, 4, 4.5, 5 (left to right and top to bottom).

agrees very well also for the pressure and velocity fields. A further investigation with the intermediate coarse grid with 64×384 cells and three levels of refinement has shown that its solution is very close to that of cases *B* and *C*. This configuration is then assumed as the base discretization for the simulations in the rest of the paper.

We remark that the use of different refinement levels does not affect substantially the CPU time and the memory needs. Furthermore, a simulation with velocity, pressure and color function fields at the same level would require, depending on the solution method, a huge amount of memory space when matrices and preconditioners are stored as sparse matrices. Higher resolutions are usually required for the color function with respect to the other fields, where the local radius of curvature of the interface is of the order of the velocity/pressure grid spacing, in order to avoid artificial breakup and numerical generation of droplets. With the multilevel approach we try to balance between these two contrasting aspects of the numerical simulations.

In Fig. 10 we show the interface profile and the pressure, color function and velocity distributions on axis at different times. The sinusoidal oscillation of the inlet velocity drives the formation of a bulge and a neck that further develop under the effect of the instability. Ultimately this leads to the formation of a droplet and a thread. At the beginning of the simulation the oscillatory behavior of both pressure and velocity is driven by the applied boundary conditions. When the thread breaks near its head, a main drop is formed that oscillates under the action of surface tension, reaching quickly a nearly spherical shape with a flat pressure profile inside, and translates with a velocity close to the inlet value U_0. The thread retreats rapidly, due to the very high value of the local curvature. Then a second breakup occurs near the tail of the thread generating a satellite droplet that contracts and expands quickly along the axis till it reaches a spherical form. During these oscillations the satellite is first reached and then absorbed by the incoming jet head. The jet evolution is almost the same if we consider higher refinement levels but during the breakup some differences do appear. It is well known that with a VOF algorithm the breakup and coalescence are automatic processes that at low resolution can change appreciably with grid refinement. In this simulation the fluid thread forms a satellite drop by breaking first near its head and then at its tail. The final satellite position depends on the timing of these two events. If the tail and the head break at the same time the droplet oscillates but its center of mass is more or less stationary; if the thread head breaks well in advance with respect to the tail, then the capillary force contracts it towards the incoming jet and the droplet is absorbed.

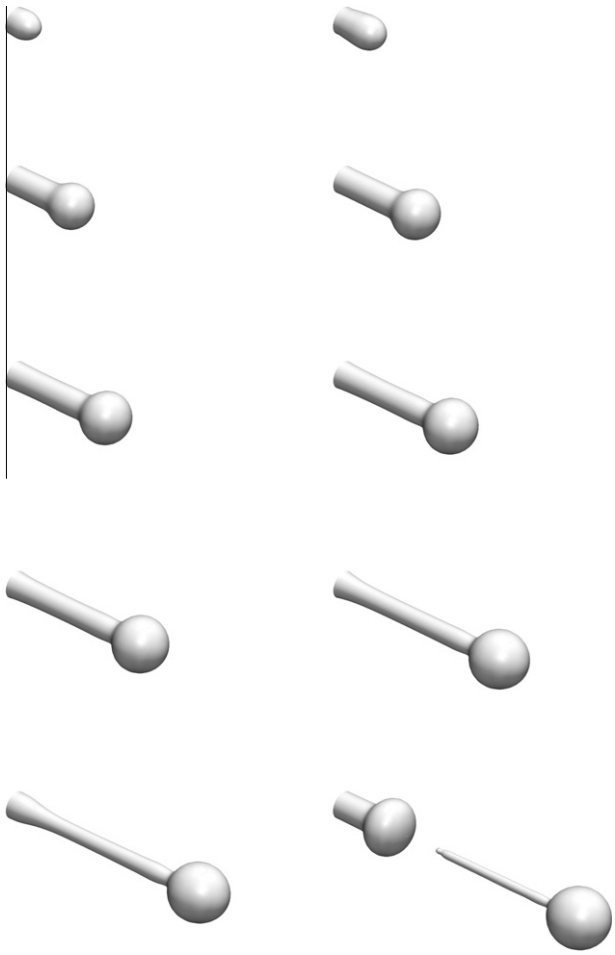

Fig. 13. Jet evolution for the longest wave length λ_3 at times 0.5, 1, 2, 2.5, 3, 3.5, 4, 5, 6, 7.5 (left to right and top to bottom).

We have performed a number of simulations with different refined meshes and can conclude that the solution shown in Fig. 10 is accurate up to the breakup. However, it is rather difficult to extrapolate the exact influence of the mesh resolution over the overall motion and in particular during the breakup. The breakup time depends on the grid spacing and a little time difference can have a relevant impact on the fast dynamics driven by the very high values of the curvature. To reduce the uncertainty in the timing of the breakup and the next fast dynamics, one should consider a higher resolution in the coarse grid, possibly with adaptive mesh refinement. Alternatively, one can introduce a breakup mechanism based on a physical model rather than an automatic geometrical process due to the mesh resolution. However, such a mechanism would probably be rather cumbersome when dealing with the three-dimensional atomization of a fast jet.

4.2.2. Pulsating jets with different wavelengths

In this section we try to reproduce sequences of physical events that are typical of a decaying liquid jet when it is forced with different wavelengths. The most significant parameter of the jet decay is the reduced wave number $kR = 2\pi R/\lambda$. At the maximum growth rate the value of kR is in the range between 0.6 and 0.7 (see Fig. 8) and the distance between the inlet section and the first drop is the shortest one. Such a distance is usually called the *breakup length*. Here we consider three different wavelengths, $\lambda_1 = 2.5 \times 10^{-3}$ m, $\lambda_2 = 3.5 \times 10^{-3}$ m and $\lambda_3 = 7.5 \times 10^{-3}$ m, while the value of the other physical quantities is that of the previous section. As a matter of fact the intermediate wavelength λ_2 is precisely that case and in Fig. 11 we see first the generation of the jet and then the formation of the main drop. The liquid bridge breaks in sequence at its head and at its tail and forms a satellite droplet. This droplet relaxes to a spherical shape and then is absorbed by the incoming jet. For this case we have $kR \approx 0.60$ and from Fig. 8 we observe that this value is very close to the reduced wave number of the maximum growth rate.

As in the previous Section 4.2.1 we consider a coarse grid with 64×384 cells, three levels of grid refinement and a non-dimensional time step $\Delta t = 1 \times 10^{-3}$. The jet evolution for the shortest wave length λ_1 is reported in Fig. 12 at different times.

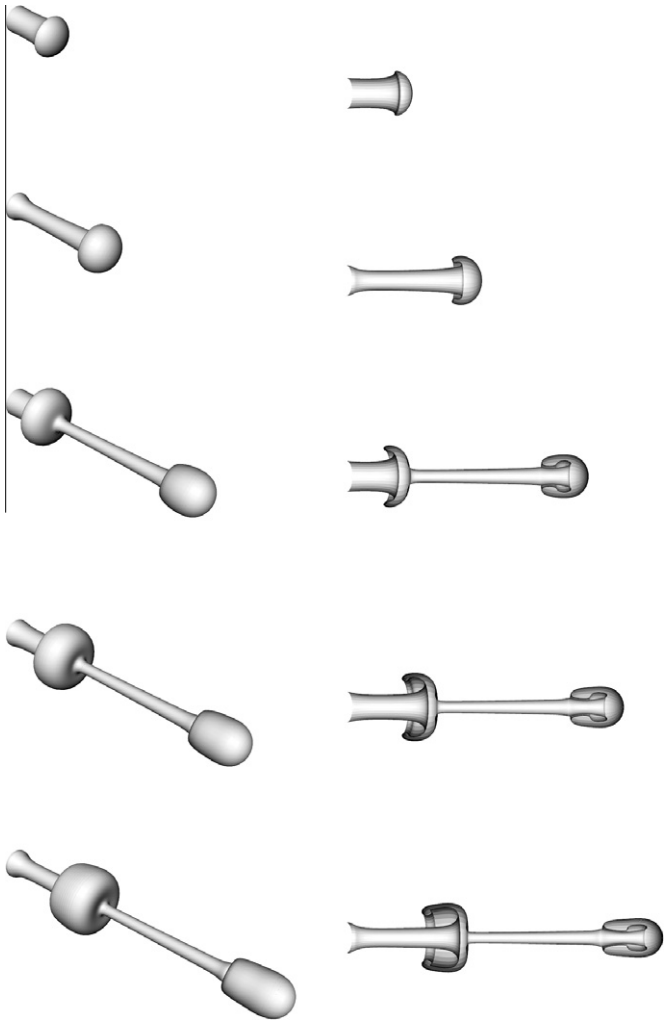

Fig. 14. Jet evolution with inlet velocity $U_0 = 10$ m/s at times 1, 2, 3.5, 4, 4.5 (two different views in each row).

After the initial growth of the instability, we observe an almost spherical drop connected by a thin thread of roughly constant thickness. The thread again breaks close to the droplet and then close to the jet. The fragment, under the action of surface tension, becomes a satellite of spherical shape but at a later time. In this case $kR = 0.825 > 0.7$ and from Fig. 8 we see that the growth rate is substantially smaller than in the previous case, the breakup length is longer and the whole process is also slower in time.

The jet evolution for the longest wave length λ_3 is reported in Fig. 13 at different times. Again, after the initial growth which is close to a sinusoidal wave, a spherical bulge develops at the end of the jet. This bulge is connected to a long and thin thread of constant thickness and now it takes quite a long time before it breaks. In this case $kR = 0.275 < 0.7$ and the corresponding growth rate is approximately half of the maximum value. The breakup length is longer than in the other two cases and the thread breaks first near its tail.

As in the previous section, by using different fine grids, we have found that the jet evolution before the breaking is accurate, but it is rather difficult to extrapolate the exact influence of the mesh resolution over the breakup mechanism which seems rather mesh dependent especially for the pulsating source with the longest wavelength where the fluid filament becomes very thin and long. The transfer operator S^{fc} is alway very small before the breaking while, close to the breaking, it increases indicating that the resolution of the interface may be not sufficient.

4.2.3. Pulsating jets with different inlet velocities

In this section we investigate the jet behavior with different inlet velocities. As we increase this velocity, turbulence becomes the dominant mechanism that governs the interface evolution. Since we are interested in direct numerical simula-

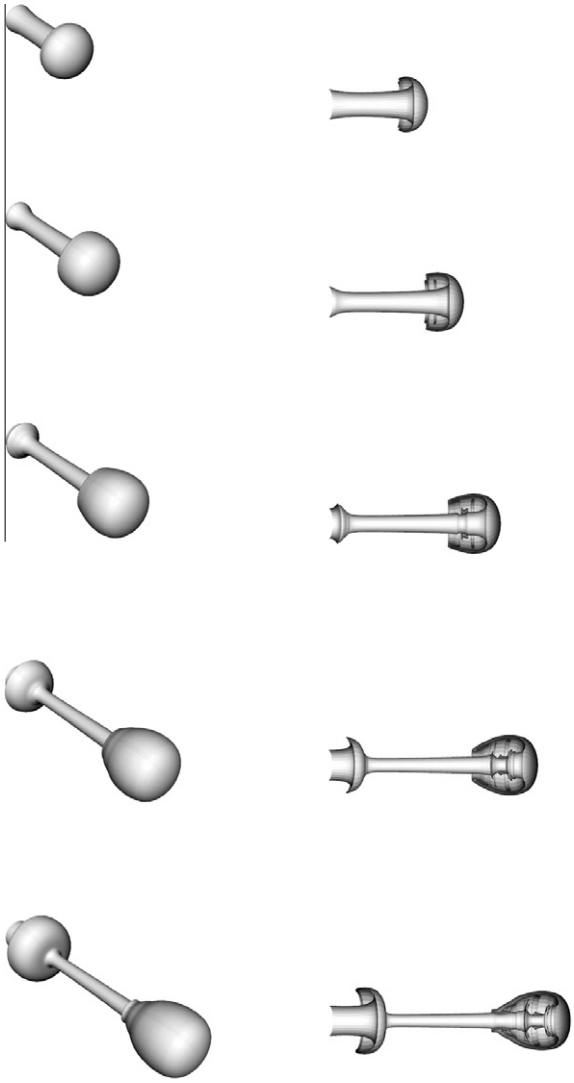

Fig. 15. Jet evolution with inlet velocity $U_0 = 100$ m/s at times 1.5, 2, 2.5, 3, 3.5 (two different views in each row).

tions, we do not consider velocity regimes that requires subgrid modeling of turbulent phenomena. We assume also that the transfer operator S^{fc} is small. This hypothesis can be evaluated *a posteriori* by a direct computation of this operator. Furthermore the prescription of turbulent inflow boundary conditions is still a challenging task when studying the initial evolution of a jet right after the nozzle exit. A very important issue in this type of simulations is the possibility to develop asymmetric instabilities. Since our simulations are axisymmetric we should avoid regimes with three-dimensional fluid structures such as fingers, filaments or secondary droplets. We can check when this happens by computing the critical Weber number We_c. Actually, turbulent and asymmetric jets are the most common and most interesting flows in engineering applications and we plan to investigate them in a different fully three-dimensional paper.

We consider two cases, one with $We < We_c$ and another one with $We > We_c$. The first case corresponds to an axisymmetric jet, the second one should develop three-dimensional structures and therefore cannot be properly simulated with an axisymmetric model. For the first case we consider a decaying jet with an oscillating inlet velocity with wavelength $\lambda = 2.5 \times 10^{-3}$ m, velocity $U_0 = 10$ m/s and amplitude $A = 0.25$. The liquid jet has density $\rho_l = 1000$ kg/m^3, viscosity $\mu_l = 0.01$ kg/ms and surface tension coefficient $\sigma = 0.0725$ J/m^2. The jet flows from a hole with diameter $D = 0.328125 \times 10^{-3}$ m into the computational domain filled with a gas with density ratio 1000 and viscosity ratio 100. With these parameters we find $Re = 328$, $We = 452$ and $Oh = 0.065$. The critical Weber number is $We_c \approx 1000$, then $We < We_c$ and an axisymmetric simulation is appropriate. The pressure and velocity fields are computed on a coarse mesh with 64×384 cells and four levels of grid refinement for the color function. The constant nondimensional time step is now $\Delta t = 1 \times 10^{-4}$. The transfer operator S^{fc} is quite small at the beginning of the simulation but becomes of appreciable size when $t > 4$, as the fluid structures near the jet head become smaller and smaller. The evolution of the interface is presented in Fig. 14 at different times. As the liquid accumulates near the jet head the forward motion produces a cylindrical sheet that surrounds the main liquid core with an interface development similar to that obtained in the Rayleigh–Taylor instability. Simulation with finer grids show that the simulation in Fig. 14 is quite accurate and no breaking appears.

In Fig. 15 we show the jet evolution for an inlet velocity $U_0 = 100$ m/s. The physical properties of the two fluids and the geometry are those of the previous case, but we have increased the surface tension coefficient, $\sigma = 1$ J/m^2. The computed Weber number is $We = 3281$ which is bigger than the critical value $We_c \approx 1000$. A simple LES model is used together with an upwind scheme to cope with the high Reynolds numbers. In Fig. 15 it is possible to see rings of fluid forming away from the interface. This is clearly not physical, since in real applications the structures that develop on the surface of high speed jets are fingers that break in very little droplets. However, these are three-dimensional structures that cannot be simulated by an axisymmetric code. In this case we do not observe convergence for the pressure and velocity fields. In fact the transfer operator (55) is large especially at times $t > 4$, when the structures inside the fluid head are quite small and fragmented. Even if the fine grid is very refined so that the interface is close to a continuous line, this is not sufficient to ensure an accurate force computation due to the small and fragmented fluid structures. In this case, the transfer operator cannot be neglected, but it should be modeled as a macroscopic term to be evaluated at the coarse level.

5. Conclusions

A multilevel VOF approach has been coupled to a robust FEM solver of the Navier–Stokes equations in axisymmetric geometry to allow two-phase flow simulations with high density ratios and a reduced amount of spurious currents. The representation of the color function over a fine grid has been introduced in order to progressively reduce the discontinuity of the interface at the cell boundary, by increasing the level of grid refinement. In the refined grid the automatic breakup and coalescence of small liquid structures occur at a spatial scale which is much smaller than the coarse grid spacing, where the pressure and velocity fields are computed. To reduce memory requirements, we have implemented on the fine grid a compact storage scheme which memorizes the color function data only in the mixed cells. A more precise computation of the capillary force is performed by using the Laplace–Beltrami operator and a volumetric approach for the two principal curvatures, respectively. Several simulations of axisymmetric jets have been performed to show the accuracy and robustness of the proposed scheme. In particular, we have first compared in a satisfactory way the numerical growth rate of several modes to its analytical value from a linear dispersion relation for axisymmetric jets. Then we have simulated a number of jets, with a given sinusoidal oscillation of the inlet velocity, to reproduce the primary breakup of the jet column by varying the frequency of the oscillation and the magnitude of the inlet velocity. The agreement with the analytical results is rather good as long as the evolution of the jet remains axisymmetric. An unphysical behavior, characterized by the formation of cylindrical structures at the jet surface, is instead shown when the Weber number exceeds the critical value. These conditions require a fully three–dimensional approach.

References

[1] W. Tauber, S.O. Unverdi, G. Tryggvason, The nonlinear behavior of a sheared immiscible fluid interface, Phys. Fluids 14 (2002) 2871–2885.
[2] G. Tryggvason, B. Bunner, A. Esmaeeli, D. Juric, N. Al-Rawahi, W. Tauber, J. Han, S. Nas, Y.-J. Jan, A front-tracking method for the computations of multiphase flow, J. Comput. Phys. 169 (2001) 708–759.
[3] R. Scardovelli, S. Zaleski, Direct numerical simulation of free-surface and interfacial flow, Annu. Rev. Fluid Mech. 31 (1999) 567–603.
[4] M. Sussman, P. Smereka, S. Osher, A level set approach for computing solutions to incompressible two-phase flow, J. Comput. Phys. 114 (1994) 146–159.

[5] T. Ménard, S. Tanguy, A. Berlemont, Coupling level set/vof/ghost fluid methods: validation and application to 3D simulation of the primary break-up of a liquid jet, Int. J. Multiphase Flow 33 (2007) 510–524.
[6] P. Marmottant, E. Villermaux, On spray formation, J. Fluid Mech. 498 (2004) 73–111.
[7] T. Boeck, J. Li, E. Lopez-Pages, P. Yecko, S. Zaleski, Ligament formation in sheared liquid–gas layers, Theor. Comput. Fluid Dyn. 21 (2007) 5976.
[8] W. Tauber, G. Tryggvason, Direct numerical simulation of primary breakup, Comput. Fluid Dyn. J. 9 (2000) 594–598.
[9] Y. Pan, K. Suga, A numerical study on the breakup process of laminar liquid jets into a gas, Phys. Fluids 18 (2006) 052101.
[10] D. Fuster, A. Bague, T. Boeck, L. Le Moyne, A. Leboissetier, S. Popinet, P. Ray, S. Scardovelli, S. Zaleski, Simulation of primary atomization with an octree adaptive mesh refinement and VOF method, Int. J. Multiphase Flow 35 (2009) 550–565.
[11] J. Eggers, E. Villermaux, Physics of liquid jets, Rep. Prog. Phys. 71 (2008) 036601.
[12] M. Gorokhovski, M. Herrmann, Modeling primary atomization, Annu. Rev. Fluid Mech. 40 (2008) 343–366.
[13] S.J. Cummins, M.M. Francois, D.B. Kothe, Estimating curvature from volume fractions, Comput. Struct. 83 (2005) 425–434.
[14] S. Popinet, An accurate adaptive solver for surface-tension-driven interfacial flows, J. Comput. Phys. 228 (2009) 5838–5866.
[15] J.H. Jeong, D.Y. Yang, Finite element analysis of transient fluid flow with free surface using VOF method and adaptive grid, Int. J. Numer. Methods Fluids 26 (1998) 1127–1154.
[16] H. Kohno, T. Tanahashi, Numerical analysis of moving interfaces using a level set method coupled with adaptive mesh refinement, Int. J. Numer. Methods Fluids 45 (2004) 921–944.
[17] L.H. Howell, J.B. Bell, An adaptive-mesh projection method for viscous incompressible flow, SIAM J. Sci. Comput. 18 (1997) 996–1013.
[18] S. Popinet, Gerris: a tree-based adaptive solver for the incompressible Euler equations in complex geometries, J. Comput. Phys. 190 (2003) 572–600.
[19] J.U. Brackbill, D.B. Kothe, C. Zemach, A continuum method for modeling surface tension, J. Comput. Phys. 100 (1992) 335–354.
[20] M. Kang, R.P. Fedkiw, X.-D. Liu, A boundary condition capturing method for multiphase incompressible flow, J. Sci. Comput. 15 (2000) 323–360.
[21] K. Goda, A multistep technique with implicit difference schemes for calculating two- or three-dimensional cavity flows, J. Comput. Phys. 30 (1979) 76–95.
[22] Y. Renardy, M. Renardy, PROST: a parabolic reconstruction of surface tension for the volume-of-fluid method, J. Comput. Phys. 183 (2002) 400–421.
[23] M.M. Francois, S.J. Cummins, E.D. Dendy, D.B. Kothe, J.M. Sicilian, M.W. Williams, A balanced-force algorithm for continuous and sharp interfacial surface tension models within a volume tracking framework, J. Comput. Phys. 213 (2006) 141–173.
[24] E. Aulisa, S. Manservisi, R. Scardovelli, A novel representation of the surface tension force for two-phase flows with reduced spurious currents, Comput. Methods Appl. Mech. Eng. 195 (2006) 6239–6257.
[25] S. Manservisi, E. Aulisa, V. Marra, R. Scardovelli, A FEM Navier–Stokes solver coupled to a front tracking algorithm for two-phase flows, in: J. Bathe (Ed.), Computational Fluid and Solid Mechanics, Elsevier, 2005, pp. 751–754.
[26] P. Gomez, J. Hernandez, J. Lopez, On the reinitialization procedure in a narrow-band locally refined level set method for interfacial flows, Int. J. Numer. Methods Eng. 63 (10) (2005) 1478–1512.
[27] M. Herrmann, A balanced force refined level set grid method for two-phase flows on unstructured flow solver grids, J. Comput. Phys. 227 (2008) 2674–2706.
[28] L.D. Landau, E.M. Lifshiftz, Mechanics, Pergamon Press, New York, 1960.
[29] R. Adams, Sobolev Spaces, Academic Press, New York, 1975.
[30] V. Girault, P. Raviart, Finite Element Method for Navier–Stokes Equations, Theory and Algorithms, Springer, New York, 1986.
[31] W.J. Rider, D.B. Kothe, Reconstructing volume tracking, J. Comput. Phys. 141 (1998) 112–152.
[32] E. Aulisa, S. Manservisi, R. Scardovelli, A mixed markers and volume-of-fluid method for the reconstruction and advection of interfaces in two-phase and free-boundary flows, J. Comput. Phys. 188 (2003) 611–639.
[33] D.J.E. Harvie, D.F. Fletcher, A new volume of fluid advection algorithm: the Stream scheme, J. Comput. Phys. 162 (2000) 1–32.
[34] Z. Bai, J. Demmel, J. Dongarra, A. Ruhe, H. van der Vorst, Templates for the Solution of Algebraic Eigenvalue Problems: A Practical Guide, SIAM, Philadelphia, 2000.
[35] J.E. Pilliod Jr., E.G. Puckett, Second-order accurate volume-of-fluid algorithms for tracking material interfaces, J. Comput. Phys. 199 (2004) 465–502.
[36] E. Aulisa, S. Manservisi, R. Scardovelli, S. Zaleski, Interface reconstruction with least-squares fit and split advection in three-dimensional Cartesian geometry, J. Comput. Phys. 225 (2007) 2301–2319.
[37] S. Gross, A. Reusken, Finite element discretization error analysis of a surface tension force in two-phase incompressible flows, SIAM J. Numer. Anal. 45 (2007) 1679–1700.
[38] S. Ganesan, G. Matthies, L. Tobiska, On spurious velocities in incompressible flow problems with interfaces, Comput. Methods Appl. Mech. Eng. 196 (2007) 1193–1202.
[39] S. Gross, A. Reusken, An extended pressure nite element space for two-phase incompressible flows with surface tension, J. Comput. Phys. 224 (2007) 40–58.
[40] S. Hysing, A new implicit surface tension implementation for interfacial flows, Int. J. Numer. Methods Fluids 51 (2006) 659–672.
[41] S. Manservisi, R. Scardovelli, A variational approach to the contact angle dynamics of spreading droplets, Comput. Fluids 38 (2009) 406–424.
[42] H.Q. Yang, Asymmetric instability of a liquid jet, Phys. Fluids 4 (1992) 681–689.
[43] Lord Rayleigh, On the instability of jets, Proc. London Math. Soc. 10 (1878) 4–15.
[44] C. Weber, Zum zerfall eines flussigkeitsstrahles, Z. Angew. Math. Mech. 11 (1931) 136–154.
[45] H. Chaves, F. Obermeier, T. Seidel, Fundamental investigations of the disintegration of a sinusoidally forced liquid jet, in: Proceedings of the Eighth International Conference on Liquid Atomization and Spray Systems, 2000, pp. 1018–1025.